A 3-D Seismic Tomographic Study of Spreading Structures and Smooth Seafloor Generated by Detachment Faulting-The Ultra-Slow Spreading Southwest Indian Ridge at 64°30'E

Adam H Robinson, Louise Watremez, Sylvie Leroy, Timothy A Minshull, Mathilde Cannat, Ana Corbalán

JGR Solid Earth

RESEARCH ARTICLE
10.1029/2024JB029253

A 3-D Seismic Tomographic Study of Spreading Structures and Smooth Seafloor Generated by Detachment Faulting—The Ultra-Slow Spreading Southwest Indian Ridge at 64° 30′E

Adam H. Robinson[1], **Louise Watremez**[2], **Sylvie Leroy**[3], **Timothy A. Minshull**[1], **Mathilde Cannat**[4], **and Ana Corbalán**[5]

[1]School of Ocean and Earth Science, University of Southampton, Southampton, UK, [2]Laboratoire d'Océanologie et de Géosciences, Université de Lille, CNRS, Université Littoral Côte d'Opale, IRD, UMR 8187, Lille, France, [3]Sorbonne Université, CNRS-INSU, Institut des Sciences de la Terre Paris, Paris, France, [4]Institut de Physique du Globe de Paris, UMR 7154 CNRS, Université Paris Cité, Paris, France, [5]Department of Earth and Environmental Sciences, Dalhousie University, Halifax, NS, Canada

Abstract At ultra-slow spreading ridges, with full spreading rates less than ~20 mm/yr, spreading is accommodated both by highly spatially and temporally segmented magmatism, and tectonic extension along large-scale detachment faults that exhume ultramafic material to the seafloor. In the most magma-poor regions, detachment faulting alternates in polarity over time, producing a "flip-flopping" effect of subsequent detachment dips. The resulting seafloor in these regions displays a morphology termed "smooth seafloor" comprising elongate, broad ridges with peridotite/serpentinite lithologies. We conducted tomographic travel-time inversion of a 3-D wide-angle seismic data set acquired over a region of smooth seafloor around 64°30′E along the Southwest Indian Ridge (SISMOSMOOTH; Cruise MD199), to produce a seismic velocity volume through the crustal section and into the uppermost mantle. We observe patterns of velocity anomalies that correspond with variations in the bathymetry arising from the mode of spreading and are interpreted as changes in the degree of alteration with depth resulting from spatial and temporal variations in fluid-rock interaction, controlled by faulting and tectonic damage processes. The detachment faults do not show simple planar structures at depth but instead mirror the shapes of the bathymetric ridges that they exhume. Magmatic input is overall highly limited, but there is one region on the lower part of an exhumed detachment footwall where a thickness of volcanic material is observed that suggests a component of syn-tectonic volcanism, which could contribute to detachment abandonment.

Plain Language Summary Ultra-slow spreading ridges are the slowest spreading type of mid-ocean ridge. At these mid-ocean ridges, instead of spreading through volcanism, the plate separation dominantly takes place along large shallow-dipping "detachment" faults. This process results in the formation of topographic ridges of "smooth seafloor" where mantle rocks are exposed. We use signals from sound sources at the sea surface recorded on receivers on the seabed to map variations in sound speed in the upper ~4 km below the seabed at an ultra-slow spreading location on the Southwest Indian Ridge. We observe patterns in the sound speed variation that we interpret in the context of spreading via detachment faults, which allow varying amounts of fluid to access the subsurface, leading to varying degrees of chemical alteration. At depth, the detachment faults show variations that mirror the shapes of the ridges they exhume, indicating that this mode of spreading is a strongly 3-D process. There is also evidence for some limited magma input in this area, some of which may have occurred during the end of the activity of a detachment fault.

Key Points:

- Ultra-slow spreading via detachment faulting producing "smooth seafloor" is a highly 3-D process
- Spatially and temporally variable fracturation and alteration of peridotites to serpentinites produces characteristic velocity patterns
- Localized lava flows and intrusions during the late stages of a detachment produce slow velocity anomalies in the upper ~1.5 km bsf

Supporting Information:

Supporting Information may be found in the online version of this article.

Correspondence to:

A. H. Robinson,
a.h.robinson@soton.ac.uk

Citation:

Robinson, A. H., Watremez, L., Leroy, S., Minshull, T. A., Cannat, M., & Corbalán, A. (2024). A 3-D seismic tomographic study of spreading structures and smooth seafloor generated by detachment faulting—The ultra-slow spreading Southwest Indian Ridge at 64°30′E. *Journal of Geophysical Research: Solid Earth*, *129*, e2024JB029253. https://doi.org/10.1029/2024JB029253

Received 5 APR 2024
Accepted 20 AUG 2024

Author Contributions:

Conceptualization: Louise Watremez, Sylvie Leroy, Mathilde Cannat
Formal analysis: Adam H. Robinson
Funding acquisition: Sylvie Leroy, Timothy A. Minshull, Mathilde Cannat
Investigation: Adam H. Robinson, Louise Watremez, Sylvie Leroy, Timothy A. Minshull, Mathilde Cannat, Ana Corbalán
Methodology: Adam H. Robinson
Writing – original draft: Adam H. Robinson

1. Introduction

The formation of the oceanic crust at fast spreading mid-oceanic ridges typically occurs as a result of plate separation driving decompression melting of the mantle, generating magma that rises toward the surface and solidifies through physical and chemical fractionation processes (e.g., Kelemen et al., 1997; Natland & Dick, 2009; Phipps Morgan & Chen, 1993). The resulting crust comprises a series of layers with differing lithological characteristics (e.g., Christeson et al., 1992; Detrick et al., 1994; Harding et al., 1993; Sinton & Detrick, 1992), that overlie a seismic discontinuity, the Moho, marking the base of the crust and the top of the

Writing – review & editing: Adam H. Robinson, Louise Watremez, Sylvie Leroy, Timothy A. Minshull, Mathilde Cannat, Ana Corbalán

lithospheric mantle (e.g., Cann, 1974; Kempner & Gettrust, 1982). The ridge full spreading rate has a significant impact on the resulting structure of the oceanic crust (e.g., Purdy et al., 1992). Global compilations of seismic and geochemical investigations across the ocean basins have found that, away from fracture zones and hotspots, below full spreading rates of 40 mm/yr (i.e., slow and ultra-slow spreading ridges) there is an increased variation in the average crustal thickness (e.g., Y. J. Chen, 1992; Christeson et al., 2019; Grevemeyer, Ranero, & Ivandic, 2018; White et al., 2001). Much of this variation is accommodated in crustal layer 3, which varies in thickness between 0.5 and 3.5 km (e.g., Jokat et al., 2003; Klingelhöfer et al., 2000), while layer 2 typically retains a relatively constant thickness of 1.5–2.5 km along-axis (Mutter & Mutter, 1993).

Along the centers of most slow and ultra-slow spreading ridge segments, plate divergence is accommodated through a combination of both magma injection and movement along moderate-offset normal faults in the axial region (Smith & Cann, 1999). By contrast, the segment ends of slow spreading ridges are characterized by large offset faults (Cann et al., 1997; Escartin et al., 2008) and broad exposures of mantle-derived serpentinized peridotites (Cannat et al., 1995). Slow spreading ridges, with a full spreading rate of ≤40 mm/yr, comprise approximately half of the 60,000 km-long global ridge system (Bird, 2003). Ultra-slow ridges (full spreading rate <20 mm/yr; Dick et al., 2003) display pronounced along-axis segmentation and represent a total length of about 12,000 km. Observations of the seismic structures of the lithosphere generated at ultra-slow spreading ridges have been made in several locations, including at the Southwest Indian Ridge (SWIR; e.g., Corbalán et al., 2021; Jian, Chen, et al., 2017; Jian, Singh, et al., 2017; Li et al., 2015; Minshull & White, 1996; Minshull et al., 2006; Momoh et al., 2017, 2020; Muller et al., 1997, 1999, 2000), ridges in the Arctic to the north of Iceland (e.g., Jokat et al., 2003, 2012; Klingelhöfer et al., 2000), and the Mid Cayman Spreading Center in the Caribbean (e.g., Peirce et al., 2019, 2022; Van Avendonk et al., 2017). The segmentation of slow and ultra-slow spreading ridges results from along-ridge variations in the magma supply, which is lower at segment ends than in the segment centers (Lin et al., 1990; Tolstoy et al., 1993). Such segment-scale variations in magma supply may be influenced by diapiric mantle upwelling (Lin et al., 1990; Parmentier & Phipps Morgan, 1990; Sparks et al., 1993) or along-axis melt migration (Cannat et al., 1999, 2003; Magde & Sparks, 1997).

Buck et al. (2005) classify oceanic crust as having been formed along a spectrum between either entirely magmatic ($M = 1$) or entirely tectonic processes ($M = 0$), where M is the fraction of the plate separation rate accommodated by magmatic diking. At the lower end of the range of M values, a significant component of the plate divergence occurs along large-offset detachment faults (Cann et al., 1997; Cannat et al., 2006; Escartín et al., 2008; MacLeod et al., 2009; Sauter et al., 2013; Smith et al., 2006). These detachment faults form at depth with initially high dip typical of normal faulting (around 70°; Martin et al., 2007; Parnell-Turner et al., 2017), before rotating about a ridge-parallel horizontal axis as in a rolling hinge model (e.g., Lavier et al., 1999). Reston and McDermott (2011) suggested that if flexure of the exhuming footwall induces strain weakening antithetic to the old fault, then the polarities of successive faults may alternate, a process termed "flip-flop" detachment faulting.

The "flip-flop" detachment model has been applied to describe the spreading patterns observed at magma-poor parts of the SWIR (Reston, 2018; Sauter et al., 2013). The type of seafloor structure resulting from this mode of spreading has been termed "smooth seafloor" (Cannat et al., 2006). This seafloor type is characterized by broad axis-parallel ridges, up to 90 km in length and 0.5–2 km in height, with a smooth, rounded topography, which may be symmetrical or steeper on their outward facing slopes (Cannat et al., 2006, 2019). Across the region mapped by Cannat et al. (2006) around 37% of the total seafloor area was of this type. Dredge samples from these locations display very high proportions of variably altered serpentinites and peridotites (Figure 1c; Sauter et al., 2013), contrasting with oceanic core complex structures along the slow spreading Mid Atlantic Ridge that expose gabbroic and basaltic rocks in addition to ultramafics (e.g., Canales et al., 2008; Cannat et al., 1995; Dick et al., 2008; Escartín et al., 2003; Ildefonse et al., 2007).

Closer to volcanic centers to the west and east, rougher seafloor fabric is observed, with inward-facing, symmetrical, moderate-offset fault scarps indicative of slow spreading oceanic crust formed by a combination of magmatism and faulting (Cannat et al., 2006, 2019). In these regions, dredged samples primarily comprise gabbros and basalts (Sauter et al., 2013). Both types of seafloor can be traced off-axis for distances greater than 100 km, indicating that the ridge processes forming them persisted over timescales of at least 11 Myr. The volcanic and smooth seafloor regions are not separated along-axis by ridge discontinuities (Cannat et al., 2019), and magnetic anomalies continue along strike between the two regions (Sauter et al., 2008). Seismicity is

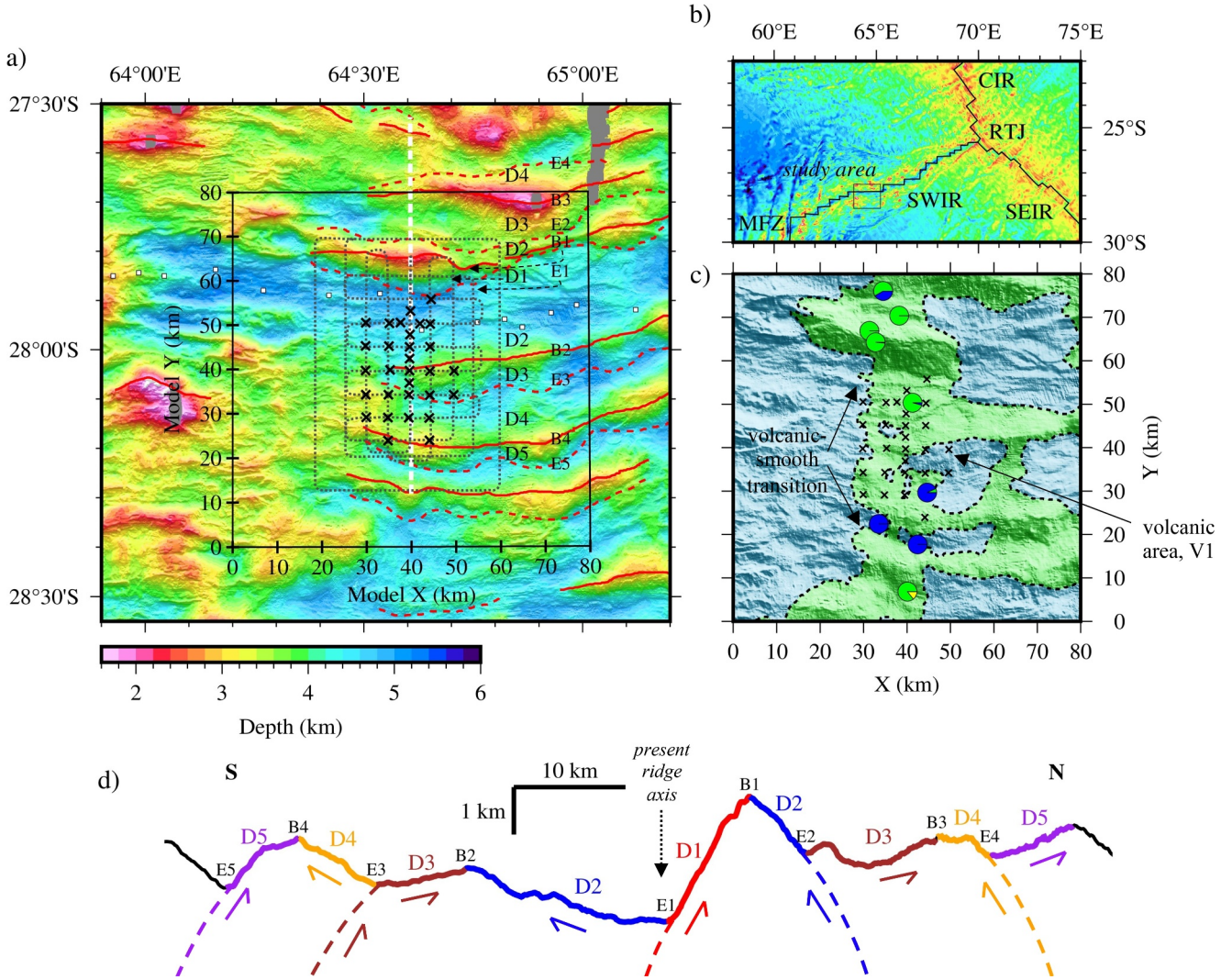

Figure 1. Location maps. (a) Ship-acquired bathymetry data over the SISMOSMOOTH study area (Cannat, 2003; Leroy & Cannat, 2014a). Black crosses are OBS locations with data used in this study, dashed gray line is the ship track over which shots were acquired. Black box shows the extent and coordinate system of the 3-D inversion modeling space. Solid red lines are the mapped fault breakaways, dashed red lines are the emergences, as in Cannat et al. (2019). Detachment phases, breakaways and emergences labeled as D, B, and E respectively, with sequence number increasing from the present-day phase 1 as in Sauter et al. (2013). White dashed line shows location of bathymetric transect shown in (d). White squares show location picks of magnetic anomaly 0 (present-day) from Cannat et al. (2006). (b) Regional bathymetry and tectonic context of eastern Southwest Indian Ridge from GEBCO (GEBCO Compilation Group, 2021). Ridge axes of the SWIR, SEIR, and CIR are plotted based on Bird (2003). Black box shows study area. SWIR—Southwest Indian Ridge, SEIR—Southeast Indian Ridge, CIR—Central Indian Ridge, RTJ—Rodriguez Triple Junction, MFZ—Melville Fracture Zone. (c) Seafloor mapped type, based on dredge sampling, seafloor morphology and backscatter analysis from Cannat et al. (2006) and Sauter et al. (2013). Blue areas are volcanic seafloor, green areas are peridotite/serpentinite. Pie charts show locations of seafloor dredges and compositions: blue = basalt, yellow = gabbro, green = peridotite/serpentinite. (d) S-N oriented bathymetric profile through $X = 40$ km, showing geometry of "flip-flop" faulting. Detachment phases paired by color as in Cannat et al. (2019), with extensions of detachments at depth shown as dashed lines with indicative dip directions. Detachment phases, breakaways and emergences labeled as in (a). Half-arrows indicate motion direction of footwalls during exhumation.

observed down to 15 km depth on-axis beneath the smooth seafloor region and its transition to more volcanic terranes (J. Chen et al., 2023), indicating that the seismogenic part of the axial lithosphere is at least that thick.

A result of the large-scale detachment, tectonically dominated mode of spreading at slow and ultra-slow spreading ridges is that some terms and concepts that have been defined for fast spread oceanic crust are no longer appropriate in these settings. Instead of the crustal section comprising a basalt-gabbro layered structure, separated from the peridotitic mantle by the Moho, it comprises materials which originated in the upper mantle prior to exhumation to shallow depths along large-offset normal faults, which become variably and heavily serpentinized through contact with seawater (e.g., Cannat, 1993; Cannat et al., 1995, 2006, 2019;

MacLeod et al., 2009; Reston & McDermott, 2011). There is a strong linear relationship between the degree of serpentinization and the lowering of seismic velocities below typical values for ultramafic materials (e.g., Carlson & Miller, 1997, 2003; Christensen, 1966, 1978, 2004; Miller & Christensen, 1997). Below this, the Moho may instead take the form of a hydration front through which the degree of serpentinization varies (e.g., Minshull et al., 1998; Muller et al., 1997, 2000). Throughout this paper we refer generally to the outer geological layer as the crustal section, regardless of its structure or composition, which lies above the seismic Moho, whether that is a discontinuity or is gradational.

In this study we investigate a segment of the SWIR that is characterized by spreading processes strongly dominated by large-scale detachment faulting ($M \sim 0$), resulting in smooth seafloor morphology at the seabed. The primary aim of this work is to further constrain the 3-D geometry of the "flip-flop" detachment faulting processes and to determine how the seismic structure of the lithosphere changes at boundaries between detachment-dominated and more magmatic ridge segments, as previously addressed using long 2-D profiles by Momoh et al. (2017) and Corbalán et al. (2021). We aim also to constrain how upper mantle rocks that are exhumed to shallow depths are altered upon contact with seawater—for example, whether the alteration is focused along the detachment faults or whether it is more pervasive. Thirdly, we seek to understand the contribution of the limited and highly segmented magma supply at ultra-slow ridges to the lifespan of the large-scale detachment faults and the structures that they generate.

To achieve the above aims, we perform 3-D travel-time tomographic inversion of signals from airgun shots recorded on an array of ocean bottom seismometers deployed at the ridge axis as part of the SISMOSMOOTH experiment (Leroy & Cannat, 2014a, 2024), to produce a seismic velocity structure for the subsurface. We then integrate this model with previous geophysical observations made in this location and compare the structure of crust formed at the ridge to that in other locations at similarly ultra-slow spreading rates.

2. Tectonic Setting

Our study area (Figure 1) is a short segment of the SWIR (segment #9 using the numbering system of Cannat et al., 1999), located between ~64°30′ and 64°42′E (Figure 1a). This segment lies within the earlier SMOOTHSEAFLOOR study area (Sauter et al., 2013). The present-day active detachment fault dips to the south and forms the axis-facing side of a ~2.5 km-high ridge (Sauter et al., 2013). Several reflector packages are observed in coincident 2-D and pseudo-3-D seismic reflection data (Momoh et al., 2017, 2020), indicating that the active detachment dips in the crust at an angle of ~50° and is associated with a km-thick domain of tectonic damage. Including the currently active fault at the ridge axis, Sauter et al. (2013) identified eight detachment phases of alternating polarity over an off-axis distance of ~80 km, corresponding to ~11 Myr of spreading history. The along-axis extent of these eight detachments ranges between 25 and 95 km (Cannat et al., 2019). Our study area focuses on the westernmost ~20–30 km of the phase 2–4 detachment structures on the southern ridge flank, following the numbering system of Sauter et al. (2013). Hereafter we refer to each detachment, fault emergence (called "termination" by many authors, e.g., Tucholke et al., 1998) and breakaway as DN, EN, and BN respectively, where N is the sequence number increasing from the presently active detachment stage D1. Figure 1d shows a N-S cross-section through the model area, displaying the geometry and nomenclature for the "flip-flopping" of detachments and resulting bathymetric features, as in Cannat et al. (2019).

Within our study area the seafloor is mostly smooth, but several regions of volcanic seafloor that rest on the ultramafic rocks exposed by the detachments have been identified using a combination of seafloor morphology and acoustic backscatter mapping and ground-truth using dredged samples (Figure 1c; Sauter et al., 2013). The largest of these is an inverted-L-shaped region located primarily on detachment surface D3 between $X = 38$–64 km and $Y = 22$–42 km (Figure 1c), and extending over the E3 emergence onto D4. Hereafter we refer to this as volcanic area V1. Another volcanic area is located on D5, with additional regions also located to the east of V1, and to the northwest of the ridge axis (Figure 1c). Several smaller volcanic patches are also present, for example, centered at: $X = 36$, $Y = 34$ km; $X = 35$, $Y = 44$ km, and; $X = 40$, $Y = 31$ km, (Figure 1c), that represent small lava flows, most likely from individual eruptive events.

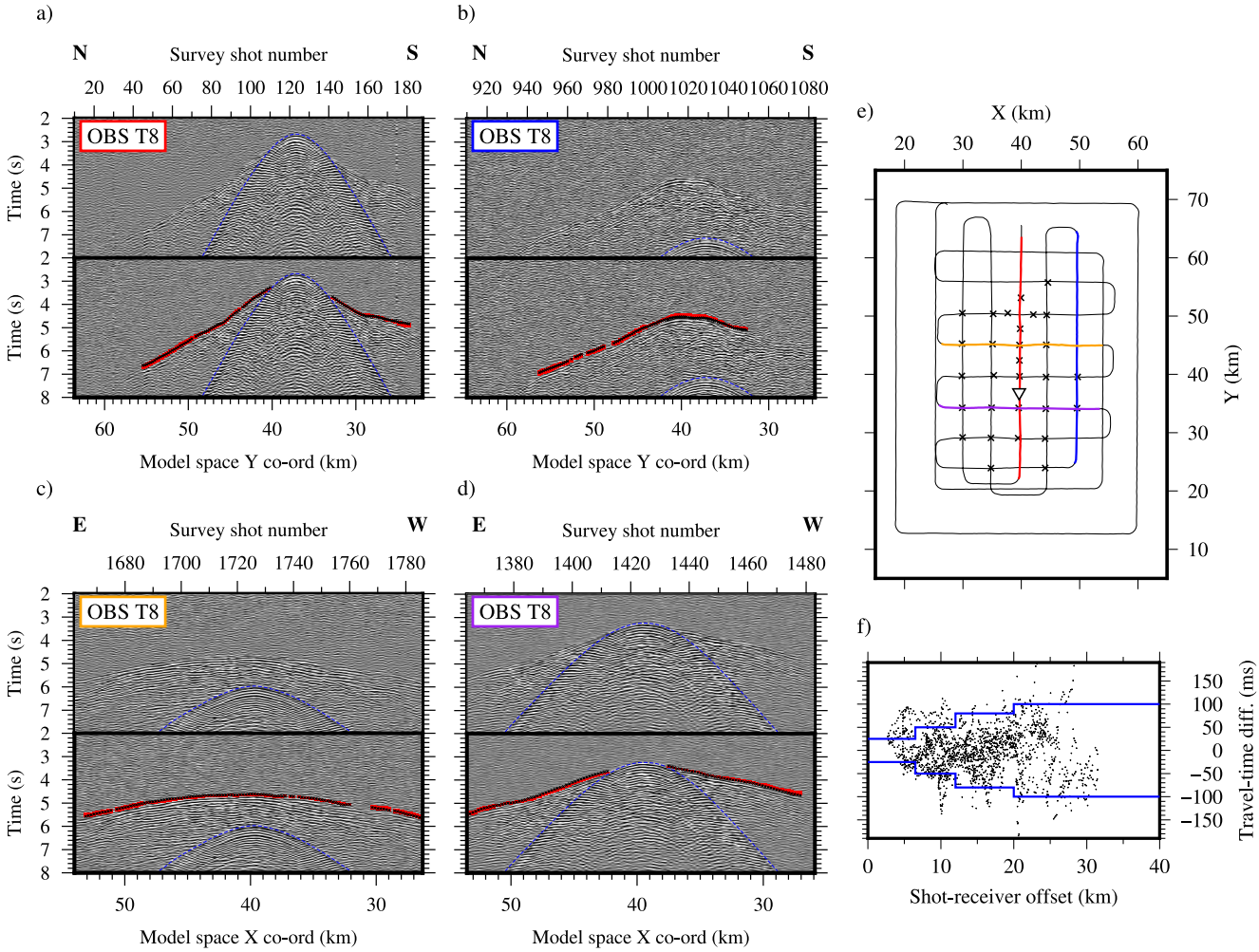

Figure 2. OBS hydrophone records for OBS T8. (a) and (b) N-S oriented profiles directly over and off-line from OBS respectively. (c) and (d) E-W oriented profiles off-line and near directly over OBS respectively. Data are shown with a 3-6-50-80 Hz bandpass filter. Upper panels show the predicted direct arrival based on OBS location as a blue line. Picks are plotted as red bars, with height corresponding to size of pick error (see Table 1). Calculated travel-times through inversion model plotted as black crosses. (e) Locations of OBSs in model coordinate system. OBS location plotted as inverted triangle, with other locations shown as black crosses, and shot acquisition track plotted as black line. Shot profiles shown in panels (a)–(d) are plotted as colored lines, color coded to panel labels. (f) Final model traced versus picked arrival travel-time residuals for all picks on OBS T8, plotted against total shot-receiver offset. Blue envelope shows the bounds of travel-time errors applied to picks with varying offset.

3. Data and Methods

3.1. SISMOSMOOTH Cruise Data

Thirty ocean bottom seismometers (OBS) collected data during the SISMOSMOOTH cruise of RV Marion Dufresne (Leroy & Cannat, 2014a, 2024) over and to the south of the ridge axis at ~64°30′E to ~64°42′E (Figure 1a). Instruments were provided by the Canadian equipment pools (Dalhousie University and the Geological Survey of Canada), INSU in France, and the National Central University, Taiwan. All instrument types recorded on four components—a hydrophone and three orthogonal geophone components—at a sampling rate of 250 Hz.

Shots were fired into these instruments using a combined Bolt/G-gun airgun source with a volume of 6,790 in^3, fired at 90 s intervals, at a depth of 10–18 m below the sea surface. Clock drift corrections were applied following GPS clock synchronization of each instrument before deployment and upon recovery. Instruments were located to their true seafloor position using a grid-search approach applied to the direct-arrival travel-times.

Table 1
Distribution of Travel-Time Errors for First Arrivals Included in Modeling

Offset range (km)	Travel-time error (ms)	Number of picks
0–6.5	25	4,914
6.5–12	50	13,217
12–20	80	16,604
>20	100	12,169
Total	–	46,904

Travel-times were picked on the hydrophone component. Example data records are shown in Figure 2 and Figures S1 and S2 in Supporting Information S1. A total of 46,904 first-arrival travel-times are included in the modeling. We do not observe extensive clear evidence for PmP reflected arrivals in the data. Travel-time errors are assigned based on shot-receiver offset (Table 1).

3.2. Tomographic Inversion

Travel-time picks were inverted in 3-D using FAST (First-Arrival Seismic Tomography; Zelt & Barton, 1998). This approach treats all arrivals as diving rays and is suitable for a data set containing only refracted arrivals and no reflections. It produces a smooth velocity model without discrete layer boundaries other than the seabed. The overall goal of an inversion is to minimize the travel-time residuals along ray paths to reach a χ^2 fit of 1, which represents a fit to the specified travel-time error bounds. If χ^2 becomes <1, the model is "relaxed" by finding the largest value of the trade-off parameter (which controls the balance between minimizing the data misfit and generating a model with the minimum required structure) that results in a χ^2 of 1.

The model was discretized at a uniform 0.1 km interval in x, y, and z, within an 80 × 80 km model footprint (Figure 1a) and extended to a depth of 15 km below the sea surface. The origin (0, 0 km in X, Y) of the model space was located at 64°12′W, 28°24′S. The seabed was constructed from swath bathymetry data (Cannat, 2003; Leroy & Cannat, 2014a). Since there is effectively no sediment cover at this location (Momoh et al., 2017, 2020), the seabed can be regarded as the top of the crustal section.

To create the starting models for inversions, a 1-D velocity-depth profile was hung below the bathymetry across the model. Our starting model was based on the two-layer approach used in the intersecting 2-D study of Corbalán et al. (2021), with the velocity control points adjusted to reduce biases in the residual travel-times. The velocity-depth points defining the starting model are given in Table 2. To reduce the effects of large second vertical derivatives of velocity, the starting model was interpolated between these points using a spline fit, which results in slightly higher velocities between the control points than would be present for a linear interpolation. The velocity profile was extended to depths greater than anticipated ray coverage by assigning a velocity gradient to produce a velocity of 8.0 km/s at 15 km bsf. Forward travel-time computation through the starting model shows that it has a starting root mean squared travel-time error (T_{rms}) of 109 ms, and a corresponding χ^2 fit of 4.26.

The inversion was run over a series of up to five non-linear iterations, with each iterating over five values of the trade-off parameter, λ, that controls the relative weighting of fitting travel-time data versus solution constraints, and which was assigned a starting value of 100 and a reduction factor of 1.41. The s_z and alpha parameters, which control respectively the relative weighting of fitting smallest versus smoothest constraint equations, and the relative importance of maintaining vertical versus horizontal smoothness, were assigned values of 0.125 and 0.9 (Zelt & Barton, 1998), and the horizontal and vertical inverse cell sizes were 1 and 0.3 km respectively. We find that the inversion rapidly converges to $\chi^2 = 1.00$, corresponding to $T_{rms} = 55$ ms, after two iterations, before continuing to $\chi^2 = 0.89$ ($T_{rms} = 53$ ms) at the end of the fifth iteration. While the χ^2 measure of fit strictly relates to cases where errors are uncorrelated, which is not necessarily the case in tomographic inversion, we choose our final model as that at the end of the second iteration, where χ^2 is first less than or equal to 1, to avoid sub-optimal performance of the FAST code at $\chi^2 < 1$. Hereafter we refer to this as the inversion model. Velocity anomalies are calculated by subtracting a mean 1-D velocity-depth profile from the inversion model, calculated using samples taken at 1 km intervals between $X = 31$–47 km and $Y = 29$–51 km (Figure 3a).

Table 2
Input 1-D Velocity-Depth Values for Starting Model and Monte Carlo Testing

Depth (km, bsf)	Velocity (km/s)	Monte Carlo depth perturbation (km)	Monte Carlo velocity perturbation (km/s)
0	3.5	±0	±0.2
2	6.4	±0.2	±0.3
5	7.5	±1	±0.3
15	8.0	±0	±0.3

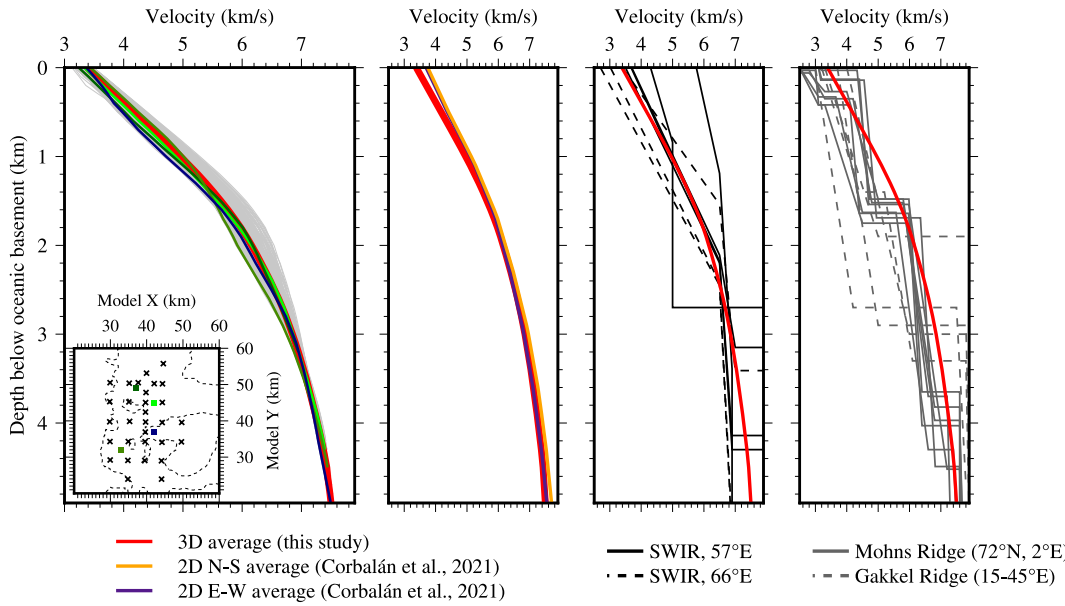

Figure 3. 1-D velocity-depth profiles. (a) 1-D velocity-depth profiles at the SISMOSMOOTH study area. Gray lines are the individual sampled 1-D profiles used for construction of the 1-D average from the 3-D inversion model, used for plotting velocity anomalies (see Section 4). Thin dark blue and green lines are 1-D samples at individual locations shown in inset map, crosses show OBS locations and dashed line is the boundary between volcanic and smooth seafloor (see Figure 1c). Red line is the 1-D average from the 3-D inversion model. (b) 1-D average from the 3-D inversion model (red) compared to N-S (orange) and E-W (purple) 1-D averages from the 2-D study of Corbalán et al. (2021). (c) 1-D velocity-depth profiles from previous studies at the SWIR—57°E (Muller et al., 2000); 66°E (Minshull et al., 2006). (d) 1-D velocity-depth profiles from previous studies at Arctic Ridges—72°N, 2°E, Mohns Ridge (Klingelhöfer et al., 2000); 15–45°E, Gakkel Ridge (Jokat et al., 2003). The average from the 3-D inversion model is shown in (c) and (d) for comparison.

1-D vertical velocity-depth profiles through our inversion model do not exhibit a vertically layered structure (Figure 3a), though we recognize that such layering could be difficult to resolve with the tomographic approach applied in this study (e.g., Zelt, 1998; Zelt & Barton, 1998). We observe a decrease in vertical velocity gradient with depth. Vertical velocity gradients in the upper ∼1.5 km of the subsurface, corresponding to absolute velocities of ≤5.5 km/s, have values of 1.2–1.6 /s and change across a ∼1.8 km-thick interval to much lower values of <0.5 /s below ∼3.3–3.4 km bsf, where the absolute velocities are generally ≥7.0 km/s. The inversion model agrees well with the 2-D results of Corbalán et al. (2021), who used a different inversion approach (Figure 3b). Mean velocities in the upper ∼1.6 km below the seafloor are up to 0.35 km/s slower in the 3-D inversion model than in the 2-D models, with the difference decreasing with increasing depth, while below this there is a good match between the two studies.

3.3. Model Testing

Testing of the 3-D inversion model is required to determine which features are robust. Zelt (1998) argues that for a 3-D tomographic inversion, horizontal resolution is primarily controlled by the ray coverage through the model, whilst vertical resolution is controlled by both the starting model used for inversion and the vertical parametrization of the inversion approach. Here we apply two types of model tests to separately appraise the horizontal resolution and velocity uncertainty of our 3-D inversion model—respectively these are checkerboard testing and Monte Carlo testing—the latter of which also allows us to appraise the suitability of our vertical parameterization.

3.3.1. Checkerboard Testing

Checkerboard testing was performed following the approach of Zelt (1998) to determine the minimum lateral size of resolvable features in the model. For each test, an alternating polarity checkerboard pattern was applied to the inversion model, where the size of the pattern discussed hereafter is that of a half-cycle, that is, a single positive or negative polarity unit. Synthetic travel-time data were calculated by forward ray-tracing through the perturbed model, and synthetic noise added to the picks, scaled according to the size of the travel-time uncertainties. These

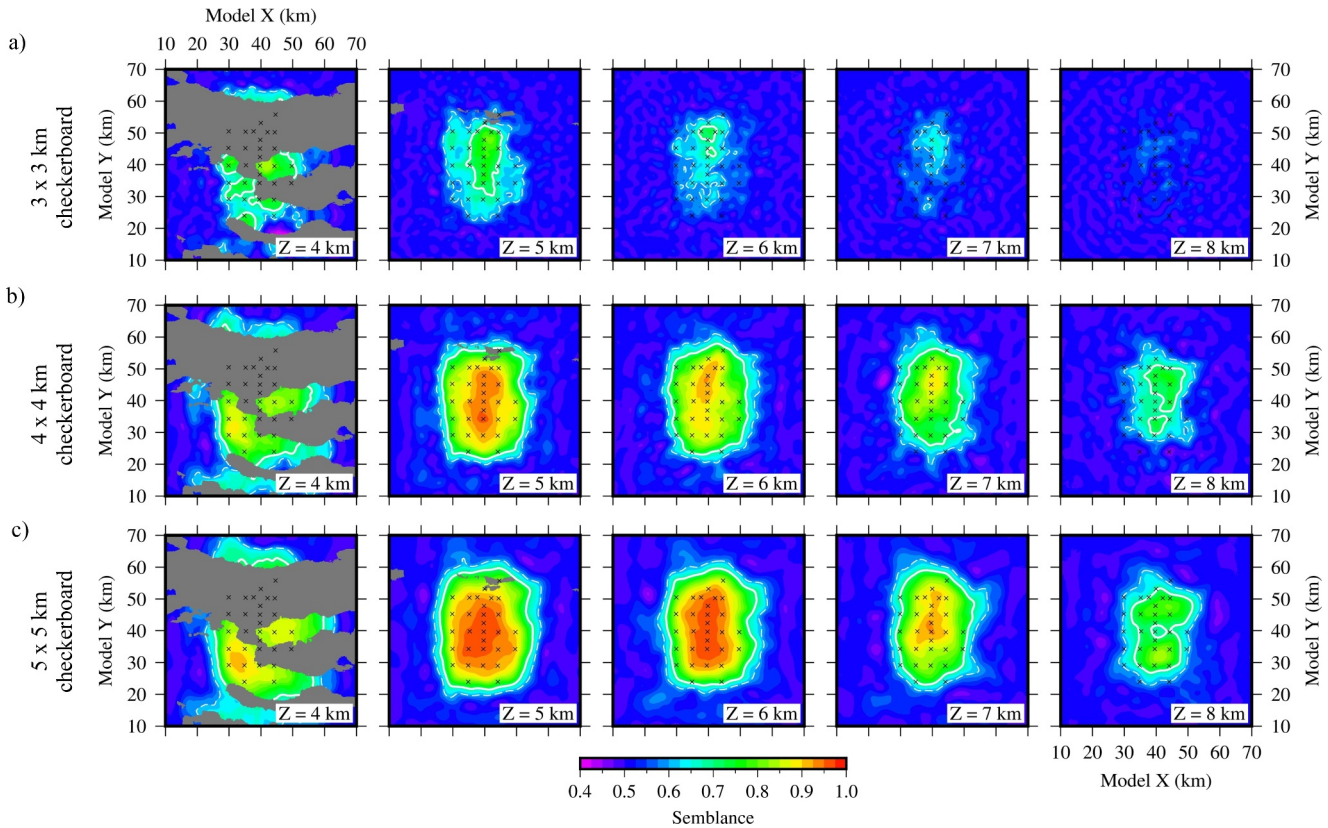

Figure 4. Averaged semblance slices from eight tested checkerboard patterns (four with phase shifts, four rotated by 45° and with phase shifts), at constant 1 km depth intervals below sea surface. (a) 3 × 3 km, (b) 4 × 4 km, and (c) 5 × 5 km average semblance, where the lateral semblance operator size in each case has size equal to the checkerboard half-cycle size (i.e., 3, 4, and 5 km respectively). Where depth slices do not intersect the subsurface, the area above the seabed is shaded gray. Solid white line indicates the 0.7 semblance contour, used by Zelt (1998) as indicator of good recovery, and dashed white line is the 0.6 semblance contour. Black crosses show OBS locations.

synthetic data were then inverted, using as a starting model the unperturbed final inversion model, to determine recovery of the applied checkerboard pattern. To best assess the horizontal resolution of the model, the checkerboard that we applied is columnar, varying in x and y but not in z (Figures S3 and S4 in Supporting Information S1, left panels; Zelt, 1998). Checkerboards were tested with a 3, 4, and 5 km unit size. We found that 4 to 5 inversion iterations are required to achieve a χ^2 of 1.

The resolvability of particular length scales can be quantified using the semblance measure of Zelt (1998), who defined a semblance threshold of 0.7 as indicating where the model was well resolved. Here we show both 0.6 and 0.7 semblance contours (Figure 4, Figures S3–S5 in Supporting Information S1). In order to account for possible effects of alignments of the checkerboard pattern nulls with acquisition lines, and directional effects, we applied multiple test runs for each checkerboard size with lateral shifts and rotations of the input pattern, and averaged the results to remove any potential effects of geometric biases (Figure S5 in Supporting Information S1).

For the 3 × 3 km checkerboard, semblance ≥0.7 is observed only at around $X = 40$ km, where the instrument spacing is smaller (Figure 4a), at depths ≤1 km bsf. For larger checkerboards, we observe that essentially the entire area beneath the footprint of the OBS array lies within the 0.7 semblance contour, down to depths of at least 7 km below sea surface for both the 4 × 4 km (Figure 4b) and 5 × 5 km checkerboards (Figure 4c), corresponding to a depth of ∼3 km bsf, extending to 8 km, or ∼4 km bsf in some areas, and locally to ∼4.6 km bsf (Figures S3 and S4 in Supporting Information S1). Overall, therefore, we can consider features with a lateral size of 5 × 5 km to be well-resolved throughout down to depths of at least ∼4 km bsf across the model area, corresponding to seismic velocities ≥7 km/s (Figure 3a), while features with a lateral size of 4 × 4 km can be resolved through to mid-crustal depths.

3.3.2. Monte Carlo Testing

Monte Carlo testing was applied to appraise the robustness of the inversion model and check for any dependence on the starting model. The testing procedure involved the generation of 100 starting models (Figure 5a), which were inverted using the same travel-time picks and parameters as the principal inversion model. The starting models were generated from the original starting model by applying perturbations drawn randomly from a uniform distribution scaled to the perturbation sizes shown in Table 2, checking to ensure that velocity increases with depth. The range of starting model χ^2 values was ∼2–15. All 100 Monte Carlo tests produced good model convergence, with χ^2 values of 1 almost always reached by the end of the second or third iteration of the inversion process (Figure 5b). A few final 1-D velocity profiles show near-zero or slightly negative vertical velocity gradients at depths ≥4–5 km bsf, which is below the depth of good ray coverage, indicating that these low gradients are most likely just inherited from starting models with slower velocities at depth (Figure 5a). These profiles do not appear to affect the robustly resolved parts of the models (Figures 5d–5g).

1-D velocity-depth profiles are taken through each of the 3-D models at the end of the second iteration at several locations (Figures 5c–5g), and the mean, standard deviation, and 68% and 95% confidence intervals calculated at 100 m depth intervals. There is overall a very good correspondence between the mean velocity from the 100 Monte Carlo tests and the velocity from the original inversion model, down to depths of at least 4 km bsf (Figures 5d–5g, left panels). Confidence intervals on the Monte Carlo mean velocity are small, at <±0.02 km/s (Figures 5d–5g, right panels). These observations indicate that there are good constraints on velocities in the upper 4 km of the basement. Below 4 km bsf we begin to observe divergence between the 1-D velocity depth profiles, and a corresponding increase in the confidence intervals, indicating that velocity constraint is reduced here, below the main extent of ray coverage. Overall there is better velocity constraint at these depths in the southern part of the model (Figures 5f and 5g) than around the ridge axis region (Figure 5d). In the ridge axis region, divergence in the individual 1-D profiles and the confidence interval on the Monte Carlo mean velocity both increase from ∼3.3 km bsf (Figure 5d), indicating that there is reduced constraint at depth in this region, arising due to fewer ray-paths at longer offsets from the north of the ridge axis. There are also variations in the Monte Carlo results in the shallowest 200 m below seabed (Figures 5d–5g). These variations occur due to a lack of refracted arrivals at the shortest offsets that leads to velocity trade-off elsewhere in the model. However, the overall tight clustering of the 1-D profiles below this region suggests that the effects of this trade-off are limited, so there is a good constraint on the velocities in the region immediately below the seabed.

Overall, our Monte Carlo testing indicates that we have good constraints on velocity through the topmost ∼4 km bsf of our model. The strong clustering of output models also provides additional confidence that the final inversion model structure is not significantly affected by the selection of the starting model. Additionally, these tests indicate that our chosen vertical model parameterization is suitable, as the output models do not display excessive vertical smoothing.

4. Results

4.1. Ridge Axis and Present-Day Spreading

The ridge axis region is characterized by an up to ∼0.2 km/s slow velocity anomaly located to the south of the present-day detachment fault emergence E1 (Figures 6a–6d and 7b, 7c, 7e, 7f; Corbalán et al., 2021; Momoh et al., 2017). The strength of the anomaly varies along-axis from west to east, though this may partially result from variations in overall model constraint as there are fewer OBSs in this part of the model. Variability in the strength of the anomaly occurs across a thickness of ≥2 km (Figure 6d), peaking between ∼0.5 and 1 km bsf (Figures 6b and 6c). The slowest anomaly appears to lie between X = 38–40 km and Y = 53–57 km, a few kilometers to the southwest of the southernmost part of the E1 emergence (Figure 6f).

At X = 40 km, the slow anomaly extends up to ∼8 km in width across-axis and over a depth interval of ∼3 km bsf (Figures 7b and 7c), with the slowest anomaly concentrated in the upper ∼1 km. To the east, at X = 45 km (Figures 7e and 7f), the slow velocity is less apparent, with thickness and magnitude of ∼1 km and <0.1 km/s respectively, and it is underlain by a faster anomaly, which trends in toward the ridge axis from the northeast at depths >1.5 km bsf (Figure 6d). To the west, toward the volcanic-smooth transition (X = 30 km), the ridge axis region has near-zero velocity anomaly over a width of ∼8 km (Figures 8b and 8c).

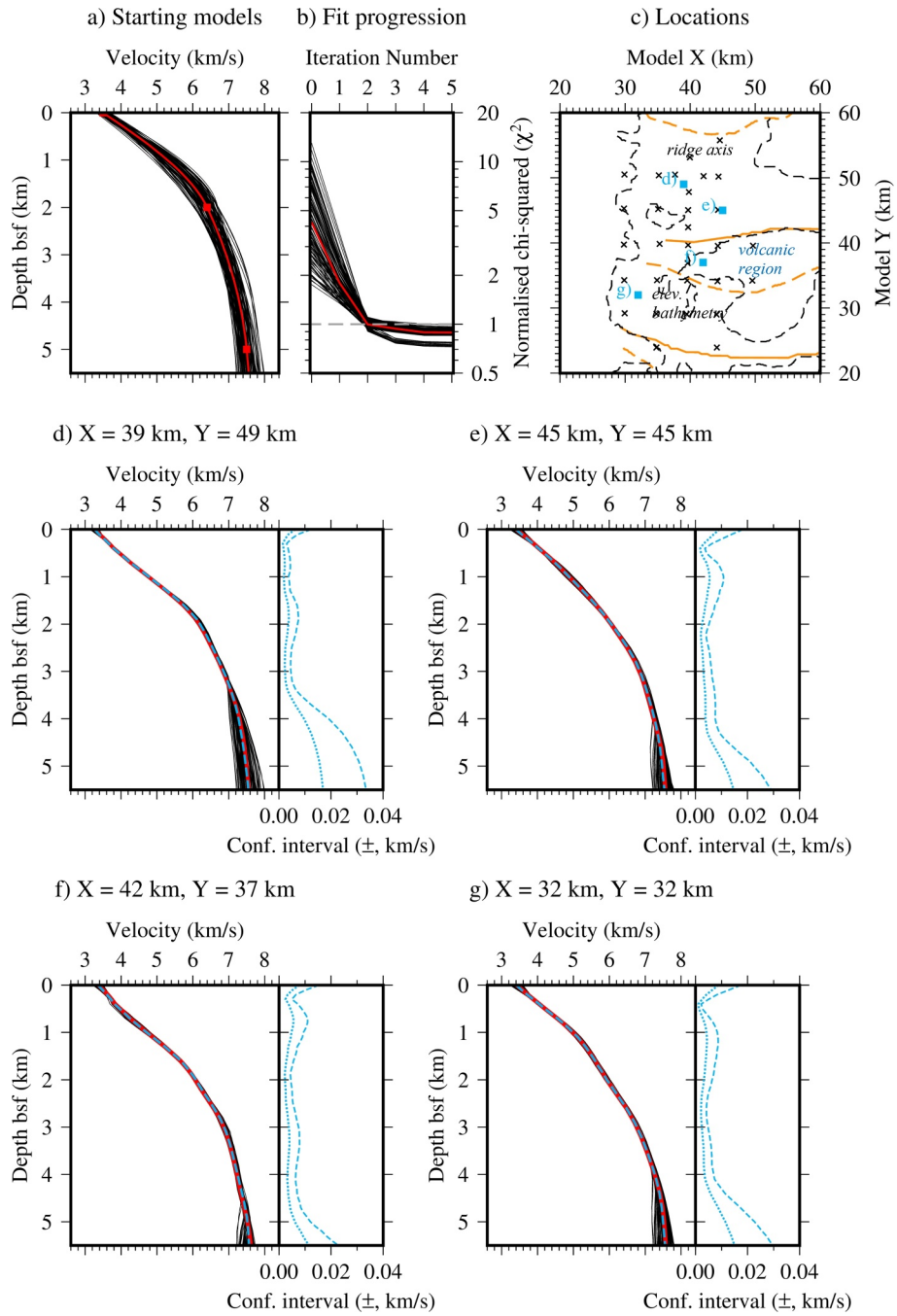

Figure 5. Monte Carlo model testing. (a) 100 starting models (black lines) are generated from the background starting model (red line) by perturbing the background control points as discussed in text and Table 2. (b) Progression of normalized chi-squared (χ^2) fit measurement from starting point (iteration 0) over five inversion iterations in FAST. Black lines are the 100 Monte Carlo model tests, red line is the background model. Dashed gray line shows $\chi^2 = 1$. (c) Locations of 1-D samples through the 3-D models, shown by blue squares and labeled with panel ids (d)–(g). Crosses are locations of the OBSs, dashed black line is the demarcation between volcanic and smooth type seafloor, and orange lines are the detachment fault emergences (dashed) and breakaways (solid). (d) 1-D velocity depth profiles through the 3-D models at model location $X = 39$ km, $Y = 49$ km. Left panel: Individual profiles shown as black lines. Red line is the structure through the background model. Dashed blue line is the average of the 100 Monte Carlo test runs. Right panel: 68% (dashed) and 95% (dotted) confidence intervals on mean 1-D velocity profile in left panel. (e)–(g) as for (d) at different locations, corresponding to different settings within the model space.

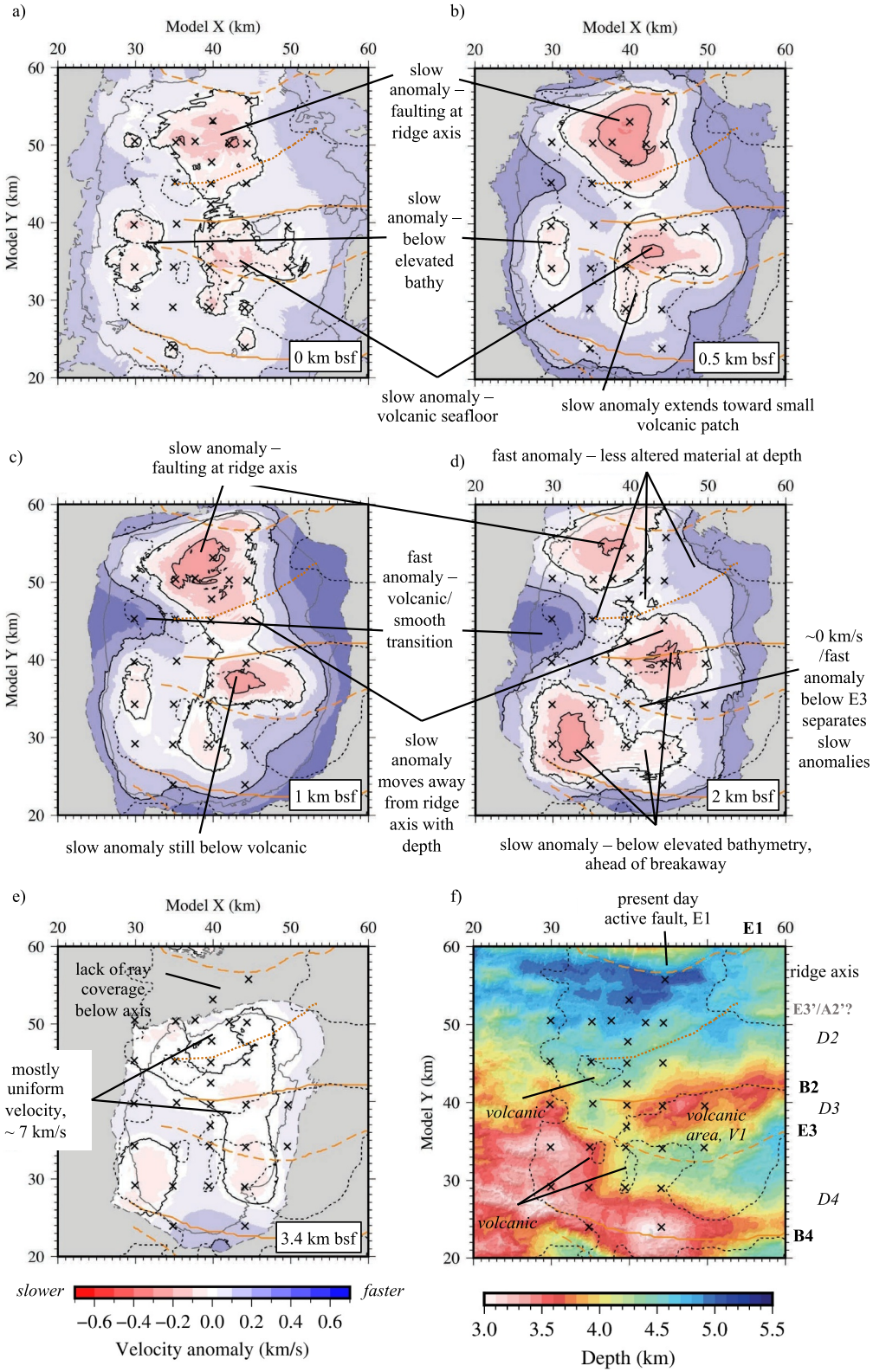

Figure 6.

4.2. Exhumation Structures

4.2.1. Detachment D2

Detachment surface D2 forms the inward-dipping, south flank of the ridge axis region, between the ridge axis and breakaway B2. The lower part of the D2 surface (Y = ~45–50 km) displays a ≤1 km-thick, up to ~0.1–0.2 km/s slow velocity anomaly below the seabed (Figures 6a–6c and 7b, 7c, 7e, 7f). This slow anomaly is underlain by an up to ~0.2 km/s faster anomaly, which varies from near-zero along X = 40 km where it is located below a slow anomaly, to a larger magnitude at X = 45 km, and corresponds to absolute velocities ≥6 km/s. In plan-view this faster anomaly forms an E-W to ENE-WSW trending band across the model area, for example, at 2 km bsf, extending into the model center from the northeast (Figure 6d).

Further south from the ridge axis, below the upper part of the D2 surface (Y = ~40–45 km), small relatively fast (0–0.1 km/s) velocity anomalies are observed in the ~1 km below the seabed (Figures 6a–6b and 7b, 7c, 7e, and 7f). Combined with the seabed slow anomaly down-dip, this corresponds to an up-dip velocity increase of ~0.1–0.2 km/s. This increase is larger than the velocity uncertainty indicated by Monte Carlo testing (e.g., Figures 5d–5g), indicating that this observation is robust. Below this, there is a 1–1.5 km-thickness, ~0.1–0.2 km/s slow velocity anomaly extending from 1 km bsf (Figure 6c), with its peak lying just to the north of breakaway B2 (Figure 6d). This region is separated from the ridge axis at depth by the ~E-W trending faster velocity anomaly.

The mapped B2 breakaway and E3 emergence features terminate at X = ~36 km and X = ~33 km respectively, to the east of the volcanic-smooth transition. In the case of B2, this is at the westernmost limit of the bathymetric ridge comprising the upper part of the D2 and D3 detachment surfaces. In this region, we observe up to ~0.2 km/s fast velocity anomalies throughout the uppermost 2 km bsf (Figures 6a–6d). The westernmost limit of the slow velocity anomaly below the upper part of the D2 surface aligns approximately with the termination of B2 (Figure 6d). This faster region separates the slow velocity anomalies associated with the D2 surface from the N-S elongate slow anomaly of up to ~0.1 km/s associated with the bathymetric high adjacent to the volcanic-smooth transition (Figures 6a–6c, 6f).

4.2.2. Detachment D3

The outward-dipping D3 surface, between emergence E3 and breakaway B2, is dominantly characterized within our model region by a large area of volcanic seafloor, V1 (see Section 4.3). At ~2 km bsf below the S-dipping E3 emergence there is an E-W oriented, slightly positive anomaly (~0.05–0.1 km/s) band which separates two broad slow velocity anomalies of up to 0.2 km/s beneath the ridge-facing upper slopes of the exposed D2 and D4 surfaces (Figure 6d, Y = 31–40 km). This feature can also be seen in cross-section along the N-S profile at X = 40 km, at Y = ~32–38 km, below a surface slow anomaly (Figures 7b and 7c). This structure lies in the footwall of the D3 detachment (Figures 7b and 7c, Y = 31–37 km, Z ~ 5 km), and is in a similar structural setting to the fast anomaly described in the lower part of the D2 footwall in Section 4.2.1.

4.2.3. Detachment D4

In the southern-central part of the model area, there is an area of E-W elongate uplifted bathymetry on the D4 surface, which has its crest along the B4 breakaway at Y = ~23 km (Figure 6f) and dips ridgeward toward emergence E3. This area connects to the west to a further large, elevated region that extends beyond the transition to volcanic seafloor, and further to the north toward the ridge axis. In the western part of our model area, volcanic area V1 extends south across the E3 emergence, onto the lower part of D4 (Figures 1c and 6f).

Between 1 and 2 km bsf, 0.05–0.25 km/s slow velocity anomalies are present beneath the N-dipping D4 surface (Figures 6c and 6d, 7b and 7c, X = 26–32 km). At shallower depths these appear as two separate low-magnitude

Figure 6. Constant depth below seafloor (bsf) slices through inversion model velocity anomaly. Depth slices at: (a) 0 km, (b) 0.5 km, (c) 1 km, (d) 2 km, and (e) 3.4 km bsf. Velocity anomaly contours at 0.2 km/s intervals. Velocity anomaly is calculated by subtracting a mean 1-D velocity profile derived from profiles sampled at 1 km intervals between X = 31–47 km and Y = 29–51 km (Figure 3a), where values are only included in the calculation where the location-depth point lies within the resolved region defined by the 0.6 semblance contour for a 5 × 5 km checkerboard size. Models are masked using the 0.6 semblance contour from eight averaged 5 × 5 km checkerboards (see Section 3.3.1), dashed gray line is the 0.6 semblance contour, solid gray line is the 0.7 semblance contour. (f) Model space bathymetry. OBS locations shown as black crosses. Solid orange lines are the mapped fault breakaways and dashed orange lines are the emergences, numbered as in Figure 1 (Cannat et al., 2019), and dotted orange line is the inferred emergence of potential detachment D3′, E3′, or antithetic fault A2′ (Corbalán et al., 2021) discussed in Section 5.4.

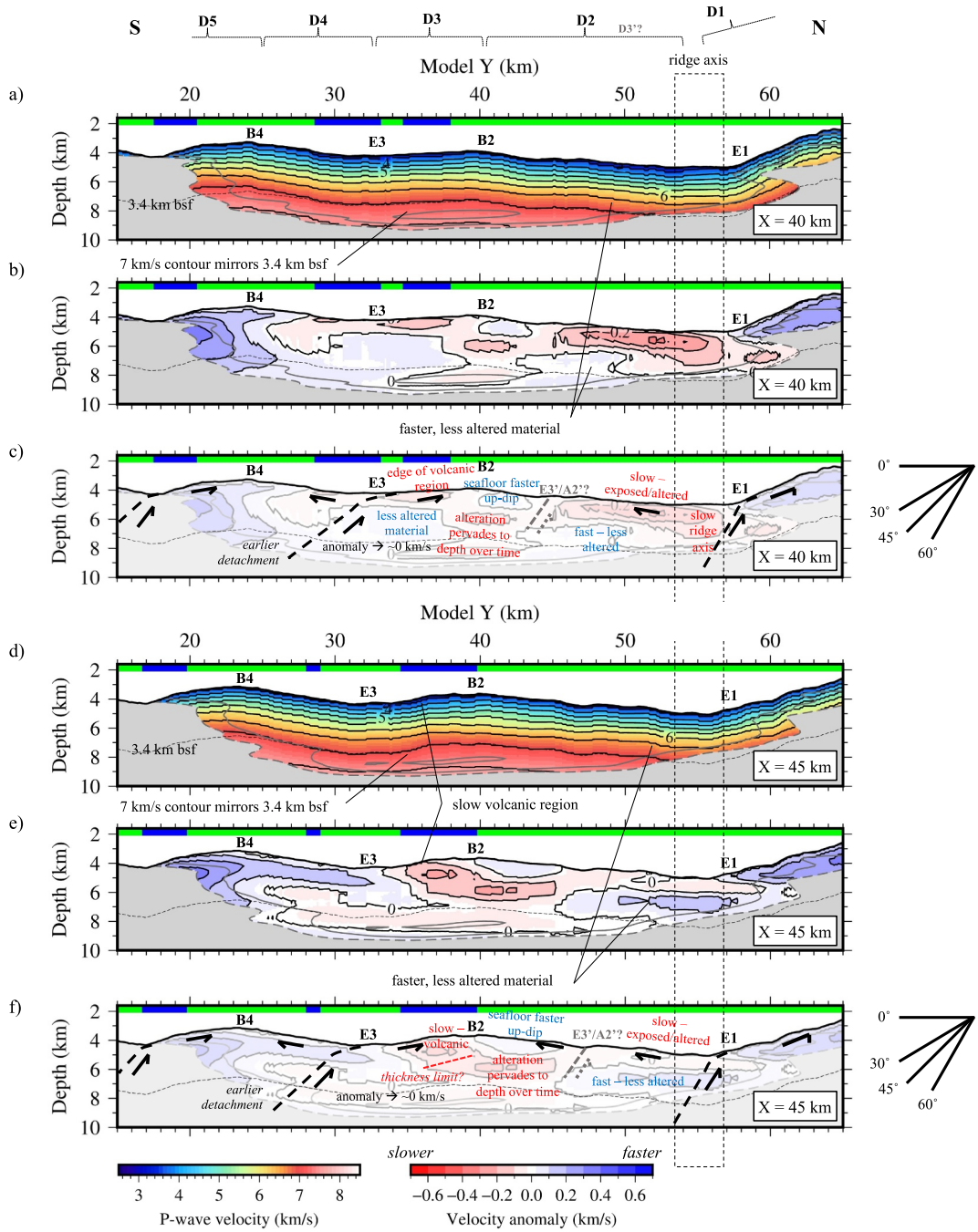

Figure 7. N-S slices through inversion model showing structures associated with exhumation mode of spreading. (a)–(c) Slices at $X = 40$ km. (a) P-wave velocity, contours at 0.5 km/s intervals. (b) Velocity anomaly relative to 1-D average velocity depth structure (see Figure 3a), contours at 0.1 km/s intervals. (c) Velocity anomaly with annotated features discussed in text. Red colors indicate slow velocities relative to the depth average, and blue colors indicate fast velocities. (d)–(f) as for (a)–(c) for slices at X = 45 km. Models are masked using the 0.6 semblance contour from eight averaged 5 × 5 km checkerboards (see Section 3.3.1), dashed gray line is the 0.6 semblance contour, solid gray line is the 0.7 semblance contour. Blue and green bars at top of panels correspond to volcanic and smooth seafloor respectively. Labels B and E show locations of fault breakaways and emergences numbered as in Figure 1. Thick dashed lines are interpreted locations of detachment faults, though dips at depth are only inferred. Half-arrows indicate motion direction of footwalls during active exhumation. Dashed gray fault with dotted motion indicator shows the location of proposed detachment and emergence D3′ and E3′, or antithetic fault A2′ discussed in Section 5.4. Thin dotted line shows 3.4 km below seabed. Panels are plotted at 1:1 aspect ratio, and a dip indicator is provided.

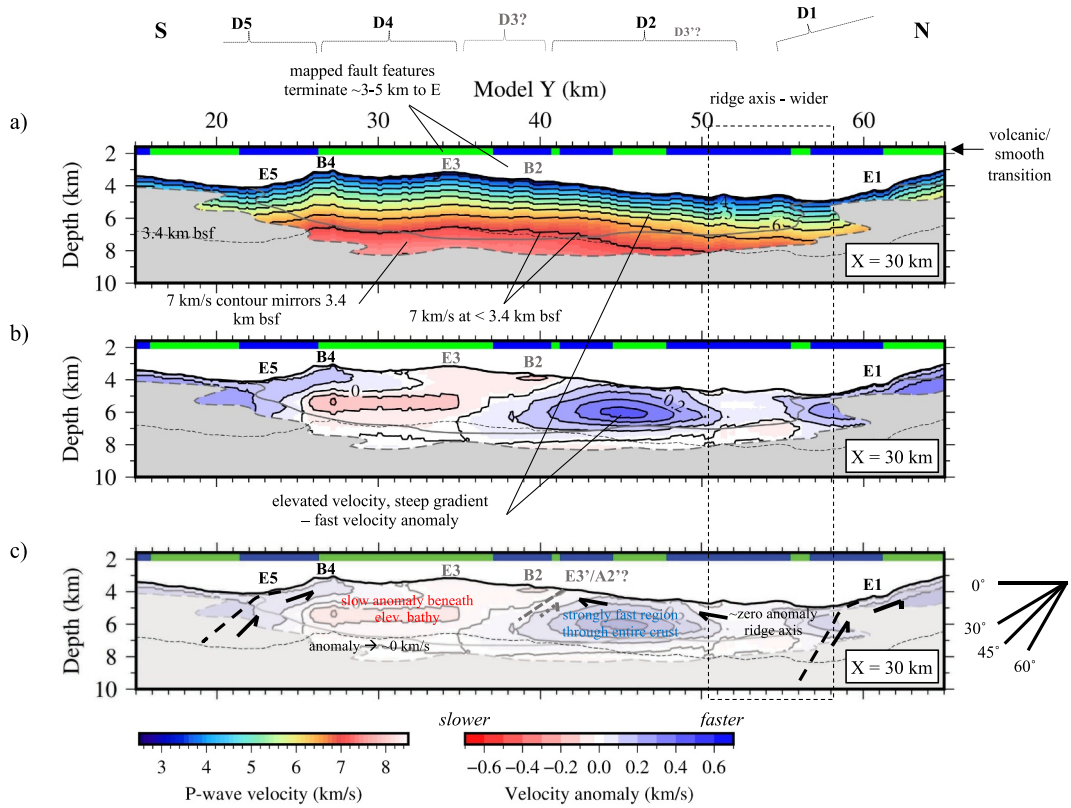

Figure 8. N-S slices through inversion model showing structures at the volcanic-smooth transition at $X = 30$ km. Panels (a)–(c) plotted as for Figures 7a–7c.

anomalies (Figure 6c), which appear to merge at depth (Figure 6d), though they retain their separate velocity minima. The stronger and more westerly of these slow anomalies, adjacent to the volcanic-smooth transition, is elongate in the N-S direction and extends further toward the ridge axis, past the termination of the E3 emergence, mirroring the bathymetry in this region (Figures 6a–6c, and 6f). This prominent elevated bathymetry displays a <0.1 km/s slow velocity anomaly between 0 and 1 km bsf at its ridge-proximal "toe" ($X \sim 40$ km), transitioning to slightly higher seabed velocities up-dip to the south (anomaly ~0–0.1 km/s, $X = 25$–30 km, Figures 6a–6c, 8b and 8c), giving a total up-dip increase of up to ~0.2 km/s.

4.3. Volcanic Area V1

Volcanic area V1 (Figure 1c) is the largest area of volcanic-type seafloor that is well resolved by our 3-D model. The P-wave velocity at the seabed inside V1 is ~3.5 km/s (Figure 9a), consistent with values for extrusive magmatic materials such as oceanic lava flows (e.g., Christeson et al., 2019). Vertical velocity gradients within volcanic area V1 are low at 0–0.4 km bsf (~0.8–1.3 /s), higher over the next ~1 km depth (~1.5–1.7 /s), and then lower again (~1 /s; Figure 3a, blue line) and overall are lower over the upper 1 km bsf compared to the smooth seafloor areas away from the ridge axis (Figure S6 in Supporting Information S1).

A 0.1–0.25 km/s slow velocity anomaly underlies the interpreted volcanic-type seafloor (Figure 9b), extending over an apparent depth interval of ~2.5 km. The boundary between the volcanic and smooth seafloor structures is well defined, with the velocity anomaly changing significantly at the edge of V1 at $X = \sim 39$ km (Figure 9b). This change can also be seen clearly in the 0, 0.5, and 1 km bsf depth slices (Figures 6a–6c).

Along $X = 45$ km, the anomalously slow area is clearly visible beneath detachment surface D3, between $Y = 35$–39 km (Figures 7e and 7f). Below the slow velocity anomaly identified in the W-E section (Figure 9), relatively slow velocities extend at a depth of ~2 km bsf toward the ridge axis to the north (Figures 6d, 7e, and 7f). We associate this deeper region of slower velocities with detachment phase D2, as discussed in Section 4.2.1. The

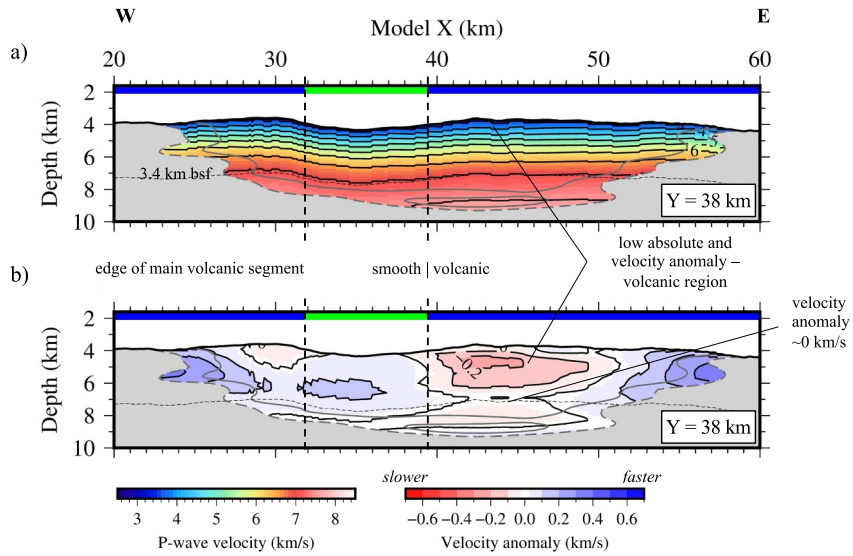

Figure 9. W-E slices at $Y = 38$ km through inversion model showing structures associated with volcanic crustal formation. (a) P-wave velocity, contours at 0.5 km/s intervals. (b) Velocity anomaly relative to 1-D average velocity depth structure (see Figure 3a), contours at 0.1 km/s intervals. Plotting and labeling as for Figure 7.

merging of these two slow anomalies can also be seen in the depth slice at 2 km bsf (Figure 6d). Thus, the slow model feature associated with volcanic area V1 has a depth extent of only ~1–1.5 km, less than would be interpreted from the W-E slice alone.

4.4. Volcanic-Smooth Transition

The transition between the areas of smooth and volcanic seafloor to the west of our study area occurs along an approximately N-S boundary at X = ~28–31 km (Figure 1c). This boundary coincides with the westernmost OBSs deployed in our study area, while two N-S shot profiles lie west of the transition (Figure 1a). Thus, while there is some recovery of subsurface structure up to 8 km west of the transition, semblance reduces with depth (Figures 4b and 4c) and the reliability of the velocities for the volcanic seafloor is limited due to the ray-paths being unidirectional. Thus, our most robust observations lie east of X = ~30 km.

At $X = 30$ km (Figure 8), the seafloor emergence of the active detachment fault on the north side of the ridge axis is ~6–7 km further north than in the center of the model area (around $X = 40$–50 km, Figures 6 and 7), resulting in an apparent widening of the ridge axis (Figures 1a and 6f). Immediately to the west of the volcanic-smooth transition, the deepest part of the ridge axis shallows by ~300 m. As a result, the mapped emergence location on the N-S profile here appears to be offset to the north of the ridge axis, the central part of which also appears to be wider than for profiles further to the east (Figure 7). In this area, the ridge axis displays a near-zero velocity anomaly across the full recovered thickness of the model (Figures 8b and 8c), though plan-view slices show that slow ridge-axis anomalies are present to the east (Figures 6a–6c) and extend into this region at 2 km bsf (Figure 6d). The lack of a clear slow anomaly here may partially be attributed to a lack of OBSs north of $Y = 51$ km in this region.

To the south of the ridge axis, there is a large anomalously fast region extending through the entire recovered thickness of the model (Figures 8b and 8c, Y ~ 40–50 km), peaking at ~0.5 km/s at ~2 km bsf. This area is also characterized by a high velocity gradient through the upper 1.5–2 km bsf (Figure 8a). The position of this anomaly aligns with the B2 breakaway (cf. Figures 7 and 8), though the mapped breakaway terminates ~5 km to the east of the volcanic-smooth transition (Figure 6f). Below and to the south of the fast region, the 7 km/s velocity contour lies shallower than 3.4 km bsf (Figure 8a). The fast region extends to the east of the transition to $X = 35$–36 km, into the smooth seafloor area (Figures 6d and 6e) terminating to the west of the mapped limit of the B2 breakaway, where the associated bathymetric ridge also terminates (Figure 6f).

4.5. Top of Weakly Hydrated Mantle Zone

Depth slices at 3.4 km bsf show approximately constant velocities of ∼7 km/s (Figure S7e in Supporting Information S1), and negligible velocity anomalies across the model area (Figure 6e). This region is also characterized by low vertical velocity gradients (Figure 3a). In N-S and W-E oriented slices the 7 km/s contour commonly lies at ∼3.4 km bsf (Figures 7a, 7d and 9a). Velocities are higher at 3.4 km bsf below and to the south of the anomalously fast region below the D2 surface at X = 30 km, along the volcanic-smooth transition (Figures 8a and 8b). At depths >3.4 km bsf, velocity anomalies are also near zero (Figures S8c and S8d in Supporting Information S1). The maximum velocities in our model are ∼7.6 km/s (Figure 3a, Figures S8a and S8b in Supporting Information S1).

4.6. Integration With MCS Observations

Coincident 2-D and pseudo-3-D seismic reflection data (Momoh et al., 2017, 2020; Figure 10a; Figures S9 and S10 in Supporting Information S1) display several reflector packages that can be associated with the faulting and associated tectonic damage during the tectonic spreading cycle in this region of the SWIR. By converting our velocity model from depth to two-way travel-time we can compare it with observations of subsurface reflectors (Figures 10b and 10c).

North-dipping packages at Y = ∼50 km do not clearly intersect the seafloor of the D2 fault surface, but do extend through to between the 6.0 and 6.5 km/s velocity contours (Figures 10a and 10b). Close to the E3 emergence at the base of the outward-facing D3 surface, the deepest packages of S-dipping reflectors penetrate through to velocities of ≥7 km/s (Figure 10b), corresponding to a depth of ∼3.4 km bsf. Profiles to the east (X = 47 km) and west (X = 32 km) of the study area show extensively distributed packages of shallow (<1 km bsf) and deeper sub-horizontal reflectors (Figures S9 and S10 in Supporting Information S1). The deeper reflectors lie at two-way times corresponding to the depths of the 7–7.5 km/s velocity contours, indicating depths ≥3.4 km bsf. Shallow sub-horizontal reflectors at Y = 25–33 km beneath the D4 surface along X = 32 km appear to lie along the top of the slow velocity anomaly at depth (Figures S9a and S9c in Supporting Information S1; cf. Figures 8b and 8c, X = 30 km).

5. Discussion

5.1. Seismic Velocity Structure and Global Ultra-Slow Ridge Context

Overall, vertical velocity gradients decrease from 1.2 to 1.6 /s in the upper ∼1.5 km of the crust to ≤0.5 /s below ∼3 km bsf, with the greatest rate of change occurring at ∼1.1–1.8 km bsf (Figure 3a). Corbalán et al. (2021) interpret this change in vertical velocity profile from lower velocity/higher gradient to higher velocity/lower gradient as a change in the porosity and permeability regime, which likely indicates the extent of tectonic damage during exhumation, and subsequently controls the degree of serpentinization with depth. The depth of the top of this gradient change corresponds to the depth of the change in the polarity with depth of the observed velocity anomalies in both the down-dip (slow anomaly at the surface, overlying a faster anomaly) and up-dip (vice versa) parts of the exhumed ultramafic basement (e.g., Figures 7b, 7c, 7e, and 7f).

Neither our model nor those of Momoh et al. (2017) and Corbalán et al. (2021, Figure 3b) show a change in velocity or velocity gradient that could be attributed to a well-defined Moho as seen at other locations along the SWIR (e.g., Minshull et al., 1998, 2006). Similarly, no Moho reflections have been observed in the 2-D (Corbalán et al., 2021; Momoh et al., 2017) and 3-D OBS data. Together, these observations are consistent with a nearly amagmatic origin for the crustal section along the smooth seafloor segments of the SWIR (Cannat et al., 2006). This conclusion is also supported by direct rock sampling, which has recovered highly and variably altered ultramafic lithologies across the smooth seafloor areas (Figure 1c; Sauter et al., 2013).

We compare the average 1-D velocity structure in our study area to velocity profiles from the Atlantis Bank, adjacent to the Atlantis II Fracture Zone at 57°15′E, to the west of our study area (Figure 3c; Muller et al., 1997, 2000), and a nearby more magmatically robust segment of the SWIR at 66°E (Figure 3c; Minshull et al., 2006). In both of these locations there is evidence for more magmatic crustal formation (intermediate M), with characteristics of oceanic layers 2 and 3 observed. Both these areas also show along-segment variations in crustal thickness, with thicker crust at segment centers and thinner crust at segment ends, and with the variation particularly focused in layer 3 (Minshull et al., 2006). Below ∼2 km bsf our model concurs with those of Momoh

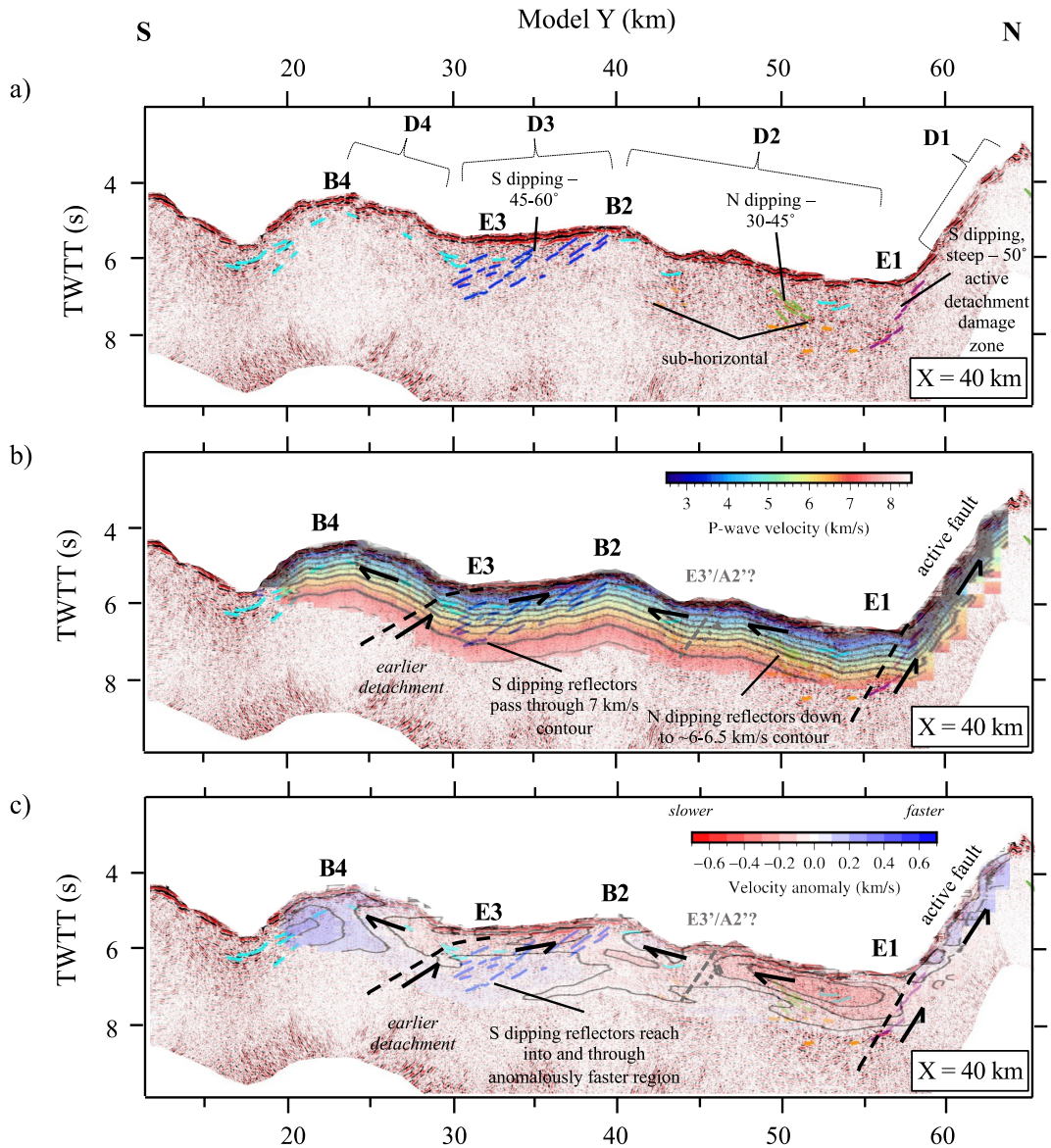

Figure 10. Comparison between 3-D tomography results and 2-D across axis MCS profile SMOO33-39. (a) Annotated seismic reflection profile with labeled breakaways, emergences, and names of exposed fault surfaces labeled. Interpreted reflectors are from Momoh et al. (2020): purple/dark blue = south dipping; green = north dipping; light blue = shallow (sub-) horizontal; orange = deeper (sub-)horizontal. See Momoh et al. (2020) for uninterpreted sections and discussion of reflector interpretations. (b) MCS data with N-S slice through 3-D model overlain ($X = 40$ km). Velocity contours drawn at 1 km/s (bold) and 0.5 km/s (thinner) intervals. (c) as for (b), with velocity anomaly, contours at 0.1 km/s intervals.

et al. (2017) and Corbalán et al. (2021) and generally shows velocities that are faster than the layer 3 velocities in these more magmatic regions.

The average 1-D structure is also similar to that of the ultra-slow Mohns Ridge in the Arctic (Figure 3d), which shows a thin (4.0 ± 0.5 km) but variable crust, with most of the variation occurring within layer 3 where this is present, and where it is absent there is a constant gradient up to relatively low upper mantle velocities of ~7.5 km/s (Klingelhöfer et al., 2000). We observe on average faster velocities than those between 15 and 45°E along the Gakkel Ridge, also in the Arctic, where the crust is observed to be very thin, between 1.9 and 3.3 km-thick, and where magma supply is interpreted to be overall limited but highly spatially segmented (Jokat et al., 2003).

5.2. Crustal Thickness and Weakly Hydrated Upper Mantle

The FAST approach to inversion used in this study does not allow the crustal thickness to be constrained directly, as it treats all rays as refracting, and does not, therefore, allow modeling of wide angle PmP reflections from the Moho, if these were present in the data. PmP phases are commonly observed in OBS records from faster spreading ridges (e.g., Canales et al., 2002; Grevemeyer et al., 1998; Holmes et al., 2008; Horning et al., 2016), and beneath magmatically spreading segments at other locations along the Mid Atlantic Ridge (e.g., Wang & Singh, 2022) and the SWIR, such as at 66°E (Minshull et al., 2006) and 50.5°E (Jian, Chen, et al., 2017), but are either absent (e.g., Mid-Cayman Spreading Center; Grevemeyer, Hayman, et al., 2018) or sparse (e.g., 13°20′N, Mid Atlantic Ridge; Simão et al., 2020) in more magma-starved areas of slow/ultra-slow spreading ridges. Due to the gradual nature of the change between the serpentinized/altered crustal section and unserpentinized mantle below, a clear seismic discontinuity that generates reflected phases is not expected to be present in our study location (e.g., Minshull et al., 1998, 2006). Moho reflections were not identified in either the pseudo-3-D MCS data set (Momoh et al., 2017) or along the two long 2-D wide-angle profiles at this location (Corbalán et al., 2021).

Therefore, we do not have a direct constraint on the thickness of the crustal section in the smooth seafloor area. As a result, we have to use other information in the form of our model testing approaches to determine to what level we can identify the base of this section. Our model testing approaches (Section 3.3) indicate that we have constraints on the velocity structure down to depths of ∼4–4.6 km bsf, and to maximum velocities of ∼7.6 km/s (Figures 4c and 5; Figures S8a and S8b in Supporting Information S1). Our velocity model also tends toward approximately zero velocity anomaly around ∼3.4 km depth bsf (Figure 6e), corresponding to absolute velocities of ∼7 km/s (Figure S7e in Supporting Information S1), except at $X = 30$ km along the volcanic-smooth transition below the D2 surface where this velocity contour is slightly shallower. Absolute velocities of ∼7–7.6 km/s correspond to ∼28% to ∼6% serpentinization of peridotites, following the linear relationship of Miller and Christensen (1997; see Section 5.3). The relative uniformity of the velocity structure below ∼3–3.4 km bsf suggests that the extent of serpentinization of the exhumed mantle at those depths is both less and less variable than in the highly damaged zone directly adjacent to the exposed detachment faults. Direct petrological constraints on serpentinization extent and temperature conditions are only available from samples that come from exposed detachment surfaces (Rouméjon et al., 2015), and are therefore not representative of serpentinization processes occurring further from the fault in the footwall and hanging wall of successive "flip-flop" detachments (see discussion in Cannat et al., 2019). Therefore, seismic data, such as presented here, are our best proxy to constrain such off-fault serpentinization.

Comparison between the velocity model and the MCS section along $X = 40$ km shows S-dipping reflectors that are interpreted as formed by damage related to detachment D3 penetrating through the 7 km/s contour into this region at depths of ∼3–3.5 km bsf (Figure 10b, $Y = 30$–35 km; Momoh et al., 2020). This comparison indicates that serpentinization associated with the D3 fault damage at those depths is not pervasive, but restricted to localized higher strain fault splays. The damage indicated by these reflectors may also possibly serve as a guide for dikes feeding the V1 volcanic area (Momoh et al., 2020). MCS profiles to the east of the study area also show extensive sub-horizontal reflectors at velocities of 7–7.5 km/s ($X = 47$ km; Figure S10 in Supporting Information S1), within the zone between the crustal section and unaltered mantle. These impedance contrasts could also result from localized serpentinization, although an origin from isolated magmatic sills in the ultramafic basement is also possible (Momoh et al., 2020).

Our maximum resolved velocities of ∼7.6 km/s are still lower than those of typical unaltered mantle (≥7.8 km/s; e.g., Christeson et al., 2019), thus suggesting that mantle hydration extends beyond ∼5 km bsf. Corbalán et al. (2021) observe more variation in the thickness of this region along their longer N-S profile across our study area, due to the length of their profiles with picked shot-receiver offsets of up to ∼90 km, which give greater constraint at depth than our model. They observe velocities increasing downward to ∼7.8 km/s by 7 km bsf, with a low velocity gradient, and sparse local regions at depth within detachment footwalls with velocity ≥8 km/s. Their model also shows less variability in velocity in the N-S direction at increasing depth below the 7 km/s contour than in the crustal section above. They also find up to ∼5% velocity difference between the N-S (faster) and E-W (slower) directions from the top of this section, decreasing to no difference at ∼6 km bsf. Their observations indicate that there may be a greater variation in the spreading processes and resulting crustal formation over longer timescales, and that the weaker alteration below ∼3.4 km bsf is controlled by a lower degree of more uniform tectonic damage than that associated with the more focused alteration around the detachments. Based on

gravity modeling, Cannat et al. (2006) inferred some variability in the crustal thickness in our study area, with thinning of up to ∼500 m relative to the reference thickness of 3.4 km (Muller et al., 1999) used in their model. However, these variations may be explained also by density variations associated with the velocity variations observed in our model.

5.3. Process and Role of Serpentinization

Sampled peridotites from slow and ultra-slow ridges are commonly observed to be extensively serpentinized, with networks of microfractures providing routes for the fluids (e.g., Andreani et al., 2007; Früh-Green et al., 2004; Rouméjon & Cannat, 2014). Observations of syn-kinematic amphiboles in sheared peridotites from the region of the SWIR studied here, which record deformation at high temperatures (>800°C), indicate that small volumes of hydrothermal fluids can penetrate as deep as the root zones of the detachments (Bickert et al., 2023). Based on the maximum depth of seismicity, this root zone is at least 15 km deep (J. Chen et al., 2023; Grevemeyer et al., 2019; Schlindwein & Schmid, 2016). In situ and bulk-rock analyses on samples from the same region of the SWIR indicate that the fluids involved in the serpentinization had compositions near seawater and oxygen isotope analyses indicate serpentinization temperatures of between 271 and 366°C (Rouméjon et al., 2015), suggesting that the extensive serpentinization documented in these samples probably develops at depth along the detachment surfaces, prior to exhumation. These reaction temperatures are consistent with the optimal serpentinization reaction temperature window of 200°C to ∼400°C (e.g., Malvoisin et al., 2012; Martin & Fyfe, 1970).

There is an approximately linear trend between serpentinization extent and P-wave velocity (e.g., Carlson & Miller, 2003; Christensen, 1966, 1978, 2004; Miller & Christensen, 1997), increasing from 0% at ∼8 km/s to 100% at ∼5 km/s, which is higher than the lowest velocities present in our model. Thus, we follow Momoh et al. (2017) and Corbalán et al. (2021) and infer that the slow velocity anomalies and absolute velocities of ≤5 km/s that we observe along the shallowest up to ∼1 km of the exposed detachment surfaces result from highly fractured serpentinized material. This interpretation is supported by observations from recovered samples (Rouméjon et al., 2015), and the MCS data which show reflectors over a 1–1.8 km-thick zone interpreted as tectonic damage around the active D1 detachment fault (Figure 10; Momoh et al., 2017, 2020). These fracture networks provide a pathway for seawater ingress into the ultramafic basement, leading to serpentinization and the generation of seismic velocity anomalies and impedance contrasts, resulting in the appearance of reflection events in the MCS data (Figure 10, Figures S9 and S10 in Supporting Information S1; Momoh et al., 2017, 2020). However, we also observe that these and similar south-dipping reflectors associated with the earlier D3 detachment cross into higher velocity domains (>7 km/s), corresponding to <∼25% serpentinized mantle (Figure 10). Thus, we suggest that the overall downward-decreasing serpentinization trend beneath the crust is dominated by low-degree serpentinization, which occurs first in the footwall and then in the hanging wall of successive "flip-flop" detachments (Cannat et al., 2019), with localized and extensively serpentinized damaged regions decreasing in frequency with greater distance from the detachments.

5.4. Tectonic Spreading Model and "Flip-Flop" Faulting

The patterns of velocity anomalies observed in the crustal section of our 3-D model can be explained through application of the "flip-flop" faulting model (Figure 1d) and the effects this has on patterns of alteration. Serpentinization is extensive across all parts of the crustal section but is focused most strongly along the detachment faults and their associated damage zones during the active stages of fault movement (Corbalán et al., 2021). This alteration is most focused at shallow depths (∼1–1.8 km), adjacent to the fault, in both the footwall and hanging wall of detachment faults, resulting in the relative slow velocity anomalies seen at and below the seafloor at the down-dip ends of exhumed footwalls, for example between Y = 45–52 km on D2 (Figures 7b, 7c, 7e, and 7f). Velocities here of <5 km/s correspond to >100% serpentinization, indicating a large degree of tectonic damage, which is supported by MCS reflection (Momoh et al., 2017, 2020) and direct sampling observations (Rouméjon et al., 2015). The extent of alteration is greater in the hanging walls of the detachments, which have a two-stage history of first being exhumed in the footwall of the earlier detachment, then remaining in a hanging wall setting for a longer time than the adjacent footwall, which progressively moves up-dip during exhumation (Cannat et al., 2019).

At greater structural depth in the paleo-ridge proximal parts of the fault footwalls we observe fast velocity anomalies associated with both detachment phases D2 (e.g., Y = 44–50 km along X = 40 km, and Y = 46–54 km

along $X = 45$ km) and D3 ($Y = 31$–37 km along $X = 40$ km, and $Y = 35$–39 km along $X = 45$ km; Figure 7) of the fault sequence, although the lowermost part of the D2 footwall is dismembered by the present-day active detachment. The strength of these anomalies is ∼0.2 and ∼<0.1 km/s respectively, with the D2 value lower than the ∼1 km/s anomaly observed in the N-S profile of Corbalán et al. (2021), which runs along $X = 40$ km. This difference may be due to increased constraint in the 2-D model from longer-offset arrivals to the north, differences in the ray-path coverage between 2-D and 3-D data, and the different inversion codes used for the two models (3-D FAST; Zelt & Barton, 1998, and tomo2d; Korenaga et al., 2000). The lower part of the exhumed structure for D4 is located outside our survey area, to the north of the ridge axis. These fast velocities at depth in the footwalls are interpreted as representing material which has undergone less alteration, due to less fluid access to these locations resulting from decreasing tectonic damage away from the detachment fault, and to shorter time periods of exposure to fluids. The depth of the transition between the slow velocity anomaly at the surface and deeper fast anomaly in the down-dip part of the exposed footwall corresponds approximately to the depth at which the vertical velocity gradient most strongly begins to decrease (Figure 3a), and to the thickness of the tectonic damage zone formed at the present-day detachment (Momoh et al., 2017, 2020), suggesting that these patterns result from a change in the degree of alteration arising from variations in the porosity regime generated through tectonic damage, which is greatest closer to the detachment fault.

Across the D2 and D4 detachment surfaces, the slow velocity anomalies shift from lying just below the seabed close to the paleo-ridge axis, for example, between $Y = 45$ and 52 km on D2 (Figures 7b, 7c, 7e, and 7f) to deeper levels up-dip toward the fault breakaway, for example, between $Y = 39$ and 44 km, suggesting that over longer time periods alteration becomes more depth-pervasive, though the alteration is also likely of a lower grade than that closer to the detachment surface due to downward decreasing tectonic damage.

Seabed velocities also appear to increase up-dip along the exposed detachment surfaces, for example, between $Y = 40$ and 45 km on D2 (Figures 7b, 7c, 7e, and 7f). While this up-dip variation is relatively small, in the region of ∼0.1 km/s, and typically the shallowest sub-seabed velocities are most sensitive to influence from the starting model velocity, our Monte Carlo testing (Section 3.3.2, Figure 5) suggests that this variation is real. This apparent up-dip increase in velocity at the seabed may arise due to relatively stronger damage in the down-dip region, including the effects of hanging wall damage processes in the following detachment phase, and/or the infilling of crack and fracture porosity by mineralization during continued hydrothermal circulation over the longer timescales over which the up-dip slope has been exposed to these processes (e.g., as documented for basaltic crust; Alt, 2004).

Corbalán et al. (2021) proposed the possible existence of an additional S-dipping detachment fault, D3′, within the inward-dipping slope on the south flank of the ridge. The inferred location of this additional detachment is shown in Figures 6, 7c, 7f, and 8c. Therefore, the fast anomaly at depth (Figures 7c and 7f, $Y = $ ∼46–53 km, ≥∼1–1.5 km bsf) may alternatively sit within the lower part of the footwall of this D3′ detachment, rather than at a similar level beneath the exposed D2 surface. However, the proposed D3′ detachment does not result in the exhumation of a large "smooth seafloor"-type ridge as seen elsewhere in our study area (Figure 1a). A small ridge (∼200 m topography) can be seen around $X = 37$–50 km, $Y = 46$–50 km (Figure 6f) and as a break in the inward-dipping exposed D2 slope (e.g., Figures 7a–7c, $Y = 46$–48 km; Figures 7d–7f, $Y = 47$–49 km). The small size of this feature was proposed to be related to a shorter timescale of exhumation (Corbalán et al., 2021). The presence of an additional large-scale detachment, D3′, to the south of the ridge does not fit the chronology of the "flip-flop" detachment sequence in this location, based on mapping of the detachment surfaces and breakaways/emergences to the north and south of the axis and constraints from magnetic anomalies (Cannat et al., 2019; Sauter et al., 2013). Instead, the small seabed ridge may be related to a relatively short-lived and small-offset S-dipping fault formed during detachment phase D2, here called A2′. These antithetic, short-lived faults are observed in numerical models of detachment systems at ultra-slow spreading ridges, where they are interpreted to represent failed attempts at polarity reversal prior to continued exhumation along the principal active detachment (Bickert et al., 2020).

While the fault breakaways are typically observed to be relatively straight, the emergences display a convex-outward "scalloped" pattern with a wavelength of ∼15–20 km, suggested to result from variations in footwall rheology which impacts the emergence angle of the fault (Cannat et al., 2019). We observe along-axis variations in the location of the buried, less-altered footwall material (fast velocity anomalies) associated with detachment phases D2 and D3, which in the case of the latter mirrors the trend of the E3 emergence at the surface, suggesting

that the complex surface shapes of the emergences extend into the subsurface. We also observe higher velocities in the subsurface at ~0.5–2 km bsf along a ~N-S trend approximately aligned with the western termination of the mapped B2 fault breakaway feature (Figures 6a–6d) and the limit of the associated bathymetric ridge (Figures 1a, 1c, and 6f), which we interpret as indicating less active alteration occurring here due to reduced fluid focusing along the fault.

The strength of the slow velocity anomaly in the hanging wall of the present-day detachment fault also appears to vary along axis, being highest between X = ~38–41 km, with the variation extending through at least 2 km thickness below the seabed (Figures 6b–6d). This slow velocity anomaly was proposed to be caused by stress holding fracture porosity open in the proximal part of the hanging wall (Momoh et al., 2017). The variation documented here may result from along-axis variations in the local stress. The peak anomaly lies close to the southernmost part of the mapped present-day fault emergence at the base of the large bathymetric ridge that bounds the ridge axis to the north (Figure 1a). This observation further supports the conclusion that the detachment faults are not simply planar at depth. It is, however, also possible that there is some bias to the velocity field due to the lower number of OBSs located immediately in this region, though the semblance measure indicates that there is still overall good resolution here.

Together these observations suggest that the geometry of detachment faults is not simply planar along-axis at depth, and that there is a link between the shape and structure of the detachment faults at depth and the morphology of the smooth seafloor which they generate through exhumation. Large-scale serpentinite-dominated detachments in other settings, for example, the Galicia margin (Lymer et al., 2019), are also observed to be non-planar, indicating that the degree of serpentinization and the geometry of detachment faulting are related (e.g., Boddupalli et al., 2022).

5.5. Volcanic-Smooth Transition

Below the volcanic-smooth transition (X = ~30 km) the velocity structure is variable. Areas at the ridge axis (Y = 50–56 km) and below the D4 detachment surface (Y = 26–40 km; Figures 8b and 8c) display patterns of velocity anomalies similar to those in equivalent settings in the smooth seafloor area to the west. However, between these features (Y = 37–51 km) there is a strong, fast velocity anomaly (Figures 6a–6d, 8b and 8c), which also has a different velocity gradient, and approaches at depth the termination of the mapped fault breakaway B2 at X = 36 km (Figures 6b–6d). The location of this fast anomaly in context of the "flip-flop" spreading and variable alteration model suggests a link with the fast anomalies in the lower part of the D2 footwall (Figure 6d), though along this region we do not find clear evidence for the S-dipping detachment D3 to separate this from the earlier detachment phase D4 (Figures 6f and 8c). Unlike further to the west, here the fast anomaly reaches the seafloor. If the protolith here comprised exhumed mantle peridotite, as across the rest of our study area, then it would be expected to have undergone significant alteration during exhumation, resulting in a slow anomaly as is seen in the smooth seafloor region to the east. Alternatively, this fast velocity anomaly may sit within the footwall of a possible E3′/A2′ fault, if this continues west to the volcanic-smooth transition. Either way, this feature does not simply fit within the model of "flip-flop" faulting and subsequent alteration that explains well the remainder of the smooth seafloor region. One possibility is that the higher velocities result from the presence of gabbroic intrusions in an oceanic core complex-type structure similar to those observed at the Mid Atlantic Ridge (e.g., Canales et al., 2008). This feature is at the edge of our well-resolved model region, so ultimately its origin cannot be confirmed.

Across-axis analysis of the bathymetry and patterns of faulting show that in the volcanic seafloor area immediately to the west of the volcanic-smooth transition, evidence for larger-scale faulting persists at least 10 km away from the transition. Thus, M is still low and the volcanic-type seafloor immediately to the west of volcanic-smooth transition in our study area is not fully characterized by normal magmatic crustal construction and is instead still strongly influenced by faulting and mantle exhumation (Cannat et al., 2019). Analysis of a long 2-D E-W wide-angle seismic profile by Corbalán et al. (2021) also found that the crustal structure varies along-axis between the two spreading mode domains over ~10 km distance. The change in crustal type in the subsurface is thus not vertically below the seafloor volcanic-smooth transition, but instead extends toward the west. This conclusion in turn suggests that the anomalous structures in this region are most likely associated with dominantly fault-driven spreading, rather than more robustly magmatic spreading. These observations provide further evidence for the 3-D nature of the detachments in this region.

5.6. Role of Volcanism in Spreading/Tectonic Cycle

Volcanic area V1 displays slow (~3.5 km/s) near-seabed velocities (Figures 3a, 7d, and 9a; Figures S7a–S7c in Supporting Information S1) consistent with extrusive basalts, and a slow velocity anomaly that appears to extend over a thickness of up to ~1–1.5 km (Figures 6a–6c, 7e, 7f, and 9b). The true thickness is likely smaller than this, and part of the slow velocity anomaly may also be contributed by mantle alteration processes. The volcanic component must, however, be thick enough to be well captured by the model, as this region displays a 0.1 km/s slower velocity anomaly than other regions characterized by shallow alteration close to the detachment (e.g., on the D2 surface between $X = 46$–49 km; Figures 7b and 7c), a 1-D velocity-depth profile distinct from that of smooth seafloor regions (Figure 3a, blue line), and a lower vertical velocity gradient across the upper ~1 km bsf (Figure S6 in Supporting Information S1). Our 1-D velocity-depth samples potentially also indicate a distinction between more extrusive and intrusive material based on a change in velocity gradient at around 0.7 km bsf (Figure 3a; Christeson et al., 1992, 2012). The thickness of this slow anomaly likely, therefore, reflects a period of magmatism that is longer than a single magmatic event creating only surface flows, but not sufficiently robust or continuous to build truly magmatic crust. Kinematic descriptions of the "flip-flop" faulting model suggest that volcanic seafloor regions may form away from their present location and be rafted into place by movement up the detachment (Reston, 2018). However, seafloor reflectivity indicates that V1 represents in situ volcanism during the late stages of activity of D3, and the onset of D2 (Sauter et al., 2013).

Variations in magma supply have been inferred to control oceanic core complex evolution along segments of the SWIR (e.g., Cannat et al., 2009; Zhou et al., 2022) and the Mid Atlantic Ridge (e.g., Escartín et al., 2017; Howell et al., 2019; Simão et al., 2020), though continued fault slip has also been inferred to occur following intrusion (Parnell-Turner et al., 2018). Changes in melt supply and focusing are significant at ultra-slow spreading ridges (e.g., Jokat et al., 2012; Klingelhöfer et al., 2000; Minshull et al., 2006; Muller et al., 1999). The segmentation at the SWIR is interpreted by Cannat et al. (2003) to arise due to local and transient increases in magma input at the base of the lithosphere, which then undergoes lateral migration along-axis. Kinematic models indicate that "flip-flop" alternating of detachment polarities remains viable with magmatic inputs up to $M = 0.5$ (Reston, 2018), supporting the possibility of syn-tectonic formation of volcanic seafloor during this process.

6. Conclusions

We have investigated the structures formed by large-scale "flip-flop" detachment faulting along a segment of the ultra-slow spreading Southwest Indian Ridge that displays characteristic smooth seafloor at the seabed, composed almost entirely of variably altered peridotites exhumed from the uppermost mantle by faulting. By applying 3-D travel-time tomography to seismic data recorded on 30 OBSs deployed over an area within and to the south of a ridge segment dominated by large-scale "flip-flop" detachment faulting we find that:

- The exhumed ultramafic footwalls of the detachment faults display patterns of seismic velocities suggesting that alteration is most strongly focused along the faults and adjacent tectonic damage zones. At depths of <~1 km bsf, velocities are lower than those that would result from 100% serpentinization, indicating both extensive alteration and tectonic damage within the fault walls during exhumation. Velocities show an apparent increase up-dip along the exhumed detachment surfaces, which may result either from relatively higher down-dip tectonic damage, which may occur during the detachment lifetime or in the hanging wall of the subsequent detachment phase, or from the progressive infilling of shallow fluid pathways by mineralization as the crust ages off-axis.
- Lower-intensity later-stage alteration penetrates to greater crustal depths up-dip in the detachment footwalls, due to the increased timescales over which alteration processes have occurred. This results in a transition from fast velocity anomalies at depth in the down-dip parts of the footwall, where there is less exposure to fluids, to slower anomalies up-dip toward the detachment breakaway. The top of this zone is demarcated by a decrease in the vertical velocity gradient, indicating a change in the porosity regime resulting from downward-decreasing tectonic damage at greater distance from the detachment fault.
- Below ~3.4 km bsf there is little spatial velocity variability across our study area, and the vertical velocity gradient is low. Here velocities increase downwards from ~7 km/s, corresponding to ~28% serpentinization, toward those of unaltered mantle compositions over a thickness of >~1.5 km, indicating a relatively spatially uniform, low degree of tectonic damage and serpentinization arising at those depths in the footwall and hanging walls of successive "flip-flop" detachments.

- The geometry of the velocity anomalies at depth varies along axis, mirroring the surface trace of the fault emergence, supporting the interpretation that the detachments are not planar at depth.
- At depth, the boundary between volcanic and ultramafic seafloor regions is more gradual than its seabed expression, consistent with geological observations pointing to a transitional region where lava flows are present overlying previously exhumed ultramafics.
- Magmatism is very limited in the smooth seafloor segments. However, the presence of a layer of magmatic origin is suggested by a slow velocity anomaly down to ∼1–1.5 km bsf within the lower part of the D3 detachment footwall, which coincides with low seafloor velocities and a low velocity gradient. The thickness of this layer is likely less than the observed extent of the velocity anomaly but greater than that generated by only surficial lava flows. Here there is likely at least some component of syn-tectonic volcanism, resulting from variations in the highly segmented along-ridge magma supply, which may have contributed to the cessation of exhumation during phase 3 of the detachment faulting sequence.

Our observations indicate that detachment-dominated spreading resulting in smooth seafloor is a spatially 3-D process, with variations in the detachment geometry observed along large-scale faulting-dominated ridge segments. There is also temporal evolution in the structure of the crust formed, both because of the "flip-flop" reversals of detachment polarity over time, and also due to varying alteration over time as exhumed ultramafic materials are exposed to seawater.

Data Availability Statement

The SISMOSMOOTH cruise data sets (Leroy & Cannat, 2014a), including multichannel seismic reflection data (Leroy & Cannat, 2014b), 3D OBS data (Leroy & Cannat, 2024) and velocity models associated with this work (Robinson et al., 2024) are available. Travel-time inversion was performed using the First-Arrival Seismic Tomography code (FAST; Zelt & Barton, 1998). Figures were generated using Generic Mapping Tools (GMT) version 6 (Wessel et al., 2019). Seismic Unix (Cohen & Stockwell, 2022) was utilized for OBS data processing and visualization.

Acknowledgments
We thank the Flotte Oceanographique Francaise (FOF) for funding the SISMOSMOOTH cruise and Institut Polaire Francais Paul Emile Victor (IPEV) for the cruise aboard the French research vessel Marion Dufresne. CNRS-INSU program Tellus provided support for the cruise and postcruise research. The work was supported by ANR projects Rift2Ridge (NT09-48546) and Ridge Factory Slow (ANR-18-CE01-0002-01). We thank the crew and scientific parties of RV Marion Dufresne cruise SISMOSMOOTH, including all technical staff. The authors acknowledge the use of the IRIDIS High Performance Computing Facility, and associated support services at the University of Southampton, in the completion of this work. We thank Harm Van Avendonk, an anonymous reviewer, and the editor and associate editor for comments that helped to improve the manuscript.

References

Alt, J. (2004). Alteration of the upper oceanic crust: Mineralogy, chemistry, and processes. In E. E. Davis & H. Elderfield (Eds.), *Hydrogeology of the oceanic lithosphere* (pp. 456–488). Cambridge University Press.

Andreani, M., Mével, C., Boullier, A. M., & Escartín, J. (2007). Dynamic control on serpentine crystallization in veins: Constraints on hydration processes in oceanic peridotites. *Geochemistry, Geophysics, Geosystems*, *8*(2), Q02012. https://doi.org/10.1029/2006GC001373

Bickert, M., Cannat, M., & Brunelli, D. (2023). Hydrous fluids down to the semi-brittle root zone of detachment faults in nearly amagmatic ultra-slow spreading ridges. *Lithos*, *442*, 107084. https://doi.org/10.1016/j.lithos.2023.107084

Bickert, M., Lavier, L., & Cannat, M. (2020). How do detachment faults form at ultraslow mid-ocean ridges in a thick axial lithosphere? *Earth and Planetary Science Letters*, *533*, 116048. https://doi.org/10.1016/j.epsl.2019.116048

Bird, P. (2003). An updated digital model of plate boundaries. *Geochemistry, Geophysics, Geosystems*, *4*(3), 1027. https://doi.org/10.1029/2001GC000252

Boddupalli, B., Minshull, T. A., Bayrakci, G., Lymer, G., Klaeschen, D., & Reston, T. J. (2022). Insights into exhumation and mantle hydration processes at the Deep Galicia Margin from a 3D high-resolution seismic velocity model. *Journal of Geophysical Research: Solid Earth*, *127*(7), e2021JB023220. https://doi.org/10.1029/2021JB023220

Buck, W. R., Lavier, L. L., & Poliakov, A. N. (2005). Modes of faulting at mid-ocean ridges. *Nature*, *434*(7034), 719–723. https://doi.org/10.1038/nature03358

Canales, J. P., Ito, G., Detrick, R. S., & Sinton, J. (2002). Crustal thickness along the western Galápagos Spreading Center and the compensation of the Galápagos hotspot swell. *Earth and Planetary Science Letters*, *203*(1), 311–327. https://doi.org/10.1016/S0012-821X(02)00843-9

Canales, J. P., Tucholke, B. E., Xu, M., Collins, J. A., & DuBois, D. L. (2008). Seismic evidence for large-scale compositional heterogeneity of oceanic core complexes. *Geochemistry, Geophysics, Geosystems*, *9*(8), Q08002. https://doi.org/10.1029/2008GC002009

Cann, J. R. (1974). A model for oceanic crustal structure developed. *Geophysical Journal of the Royal Astronomical Society*, *39*(1), 169–187. https://doi.org/10.1111/j.1365-246x.1974.tb05446.x

Cann, J. R., Blackman, D. K., Smith, D. K., McAllister, E., Janssen, B., Mello, S., et al. (1997). Corrugated slip surfaces formed at ridge–transform intersections on the Mid-Atlantic Ridge. *Nature*, *385*(6614), 329–332. https://doi.org/10.1038/385329a0

Cannat, M. (1993). Emplacement of mantle rocks in the seafloor at mid-ocean ridges. *Journal of Geophysical Research*, *98*(B3), 4163–4172. https://doi.org/10.1029/92jb02221

Cannat, M. (2003). *MD 135/SWIR 61-65 cruise*. RV Marion Dufresne. https://doi.org/10.17600/3200080

Cannat, M., Céline, R. J., & Fujimoto, H. (2003). Melt supply variations to a magma-poor ultra-slow spreading ridge (Southwest Indian Ridge 61° to 69°E). *Geochemistry, Geophysics, Geosystems*, *4*(8), 1–21. https://doi.org/10.1029/2002GC000480

Cannat, M., Karson, J. A., Miller, D. J., Agar, S. M., Barling, J., Casey, J. F., et al. (1995). In *Proceedings of the Ocean Drilling Program, Init. Repts* (Vol. 153). Ocean Drilling Program. https://doi.org/10.2973/odp.proc.ir.153.1995

Cannat, M., Rommevaux-Jestin, C., Sauter, D., Deplus, C., & Mendel, V. (1999). Formation of the axial relief at the very slow spreading Southwest Indian Ridge (49°–69°E). *Journal of Geophysical Research*, *104*(B10), 22825–22843. https://doi.org/10.1029/1999JB900195

Cannat, M., Sauter, D., Escartín, J., Lavier, L., & Picazo, S. (2009). Oceanic corrugated surfaces and the strength of the axial lithosphere at slow spreading ridges. *Earth and Planetary Science Letters*, *288*(1–2), 174–183. https://doi.org/10.1016/j.epsl.2009.09.020

Cannat, M., Sauter, D., Lavier, L., Bickert, M., Momoh, E., & Leroy, S. (2019). On spreading modes and magma supply at slow and ultraslow mid-ocean ridges. *Earth and Planetary Science Letters*, *519*, 223–233. https://doi.org/10.1016/j.epsl.2019.05.012

Cannat, M., Sauter, D., Mendel, V., Ruellan, E., Okino, K., Escartín, J., et al. (2006). Modes of seafloor generation at a melt-poor ultraslow-spreading ridge. *Geology*, *34*(7), 605–608. https://doi.org/10.1130/G22486.1

Carlson, R. L., & Miller, D. J. (1997). A new assessment of the abundance of serpentinite in the oceanic crust. *Geophysical Research Letters*, *24*(4), 457–460. https://doi.org/10.1029/97GL00144

Carlson, R. L., & Miller, D. J. (2003). Mantle wedge water contents estimated from seismic velocities in partially serpentinized peridotites. *Geophysical Research Letters*, *30*(5), 1250. https://doi.org/10.1029/2002gl016600

Chen, J., Crawford, W. C., & Cannat, M. (2023). Microseismicity and lithosphere thickness at a nearly-amagmatic oceanic detachment fault system. *Nature Communications*, *14*(1), 430. https://doi.org/10.1038/s41467-023-36169-w

Chen, Y. J. (1992). Oceanic crustal thickness versus spreading rate. *Geophysical Research Letters*, *19*(8), 753–756. https://doi.org/10.1029/92GL00161

Christensen, N. I. (1966). Elasticity of ultrabasic rocks. *Journal of Geophysical Research*, *71*(24), 5921–5931. https://doi.org/10.1029/JZ071i024p05921

Christensen, N. I. (1978). Ophiolites, seismic velocities and oceanic crustal structure. *Tectonophysics*, *47*(1–2), 131–157. https://doi.org/10.1016/0040-1951(78)90155-5

Christensen, N. I. (2004). Serpentinites, peridotites, and seismology. *International Geology Review*, *46*(9), 795–816. https://doi.org/10.2747/0020-6814.46.9.795

Christeson, G. L., Goff, J. A., & Reece, R. S. (2019). Synthesis of oceanic crustal structure from two-dimensional seismic profiles. *Reviews of Geophysics*, *57*(2), 504–529. https://doi.org/10.1029/2019RG000641

Christeson, G. L., Morgan, J. V., & Warner, M. R. (2012). Shallow oceanic crust: Full waveform tomographic images of the seismic layer 2A/2B boundary. *Journal of Geophysical Research*, *117*(B5), B05101. https://doi.org/10.1029/2011JB008972

Christeson, G. L., Purdy, G. M., & Fryer, G. J. (1992). Structure of young upper crust at the East Pacific Rise near 9°30′N. *Geophysical Research Letters*, *19*(10), 1045–1048. https://doi.org/10.1029/91GL00971

Cohen, J. K., & Stockwell, J. W., Jr. (2022). *CWP/SU: Seismic Un*x release No. 44R26: An open source software package for seismic research and processing*. Center for Wave Phenomena, Colorado School of Mines.

Corbalán, A., Nedimović, M. R., Louden, K. E., Cannat, M., Grevemeyer, I., Watremez, L., & Leroy, S. (2021). Seismic velocity structure along and across the ultraslow-spreading Southwest Indian Ridge at 64°30′E showcases flipping detachment faults. *Journal of Geophysical Research: Solid Earth*, *126*(10), 1–24. https://doi.org/10.1029/2021JB022177

de Martin, B. J., Sohn, R. A., Canales, J. P., & Humphris, S. E. (2007). Kinematics and geometry of active detachment faulting beneath the Trans-Atlantic Geotraverse (TAG) hydrothermal field on the Mid-Atlantic Ridge. *Geology*, *35*(8), 711–714. https://doi.org/10.1130/G23718A.1

Detrick, R., Collins, J., Stephen, R., & Swift, S. (1994). In situ evidence for the nature of the seismic layer 2/3 boundary in oceanic crust. *Nature*, *370*(6487), 288–290. https://doi.org/10.1038/370288a0

Dick, H. J., Lin, J., & Schouten, H. (2003). An ultraslow-spreading class of ocean ridge. *Nature*, *426*(6965), 405–412. https://doi.org/10.1038/nature02128

Dick, H. J., Tivey, M. A., & Tucholke, B. E. (2008). Plutonic foundation of a slow-spreading ridge segment: Oceanic core complex at Kane Megamullion, 23 30′N, 45 20′W. *Geochemistry, Geophysics, Geosystems*, *9*(5), Q05014. https://doi.org/10.1029/2007GC001645

Escartín, J., Mével, C., MacLeod, C. J., & McCaig, A. M. (2003). Constraints on deformation conditions and the origin of oceanic detachments: The Mid-Atlantic Ridge core complex at 15°45′N. *Geochemistry, Geophysics, Geosystems*, *4*(8), 1067. https://doi.org/10.1029/2002GC000472

Escartín, J., Mével, C., Petersen, S., Bonnemains, D., Cannat, M., Andreani, M., et al. (2017). Tectonic structure, evolution, and the nature of oceanic core complexes and their detachment fault zones (13° 20′N and 13° 30′N, Mid Atlantic Ridge). *Geochemistry, Geophysics, Geosystems*, *18*(4), 1451–1482. https://doi.org/10.1002/2016GC006775

Escartín, J., Smith, D. K., Cann, J., Schouten, H., Langmuir, C. H., & Escrig, S. (2008). Central role of detachment faults in accretion of slow-spreading oceanic lithosphere. *Nature*, *455*(7214), 790–794. https://doi.org/10.1038/nature07333

Früh-Green, G. L., Connolly, J. A. D., Plas, A., Kelley, D. S., & Grobéty, B. (2004). Serpentinization of oceanic peridotites: Implications for geochemical cycles and biological activity. *Geophysical Monograph Series*, *144*, 119–136. https://doi.org/10.1029/144GM08

GEBCO Compilation Group. (2021). GEBCO 2021 grid. https://doi.org/10.5285/c6612cbe-50b3-0cff-e053-6c86abc09f8f

Grevemeyer, I., Hayman, N. W., Lange, D., Peirce, C., Papenberg, C., Van Avendonk, H. J. A., et al. (2019). Constraining the maximum depth of brittle deformation at slow- and ultraslow-spreading ridges using microseismicity. *Geology*, *47*(11), 1069–1073. https://doi.org/10.1130/G46577.1

Grevemeyer, I., Hayman, N. W., Peirce, C., Schwardt, M., Van Avendonk, H. J. A., Dannowski, A., & Papenberg, C. (2018). Episodic magmatism and serpentinized mantle exhumation at an ultraslow-spreading centre. *Nature Geoscience*, *11*(6), 444–448. https://doi.org/10.1038/s41561-018-0124-6

Grevemeyer, I., Ranero, C. R., & Ivandic, M. (2018). Structure of oceanic crust and serpentinization at subduction trenches. *Geosphere*, *14*(2), 395–418. https://doi.org/10.1130/GES01537.1

Grevemeyer, I., Weigel, W., & Jennrich, C. (1998). Structure and ageing of oceanic crust at 14°S on the East Pacific Rise. *Geophysical Journal International*, *135*(2), 573–584. https://doi.org/10.1046/j.1365-246X.1998.00673.x

Harding, A. J., Kent, G. M., & Orcutt, J. A. (1993). A multichannel seismic investigation of upper crustal structure at 9°N on the East Pacific Rise: Implications for crustal accretion. *Journal of Geophysical Research*, *98*(B8), 13925–13944. https://doi.org/10.1029/93JB00886

Holmes, R. C., Tolstoy, M., Cochran, J. R., & Floyd, J. S. (2008). Crustal thickness variations along the Southeast Indian Ridge (100–116°E) from 2-D body wave tomography. *Geochemistry, Geophysics, Geosystems*, *9*(12), Q12020. https://doi.org/10.1029/2008GC002152

Horning, G., Canales, J. P., Carbotte, S. M., Han, S., Carton, H., Nedimović, M. R., & Van Keken, P. E. (2016). A 2-D tomographic model of the Juan de Fuca plate from accretion at axial seamount to subduction at the Cascadia margin from an active source ocean bottom seismometer survey. *Journal of Geophysical Research: Solid Earth*, *121*(8), 5859–5879. https://doi.org/10.1002/2016JB013228

Howell, S., Olive, J.-A., Ito, G., Behn, M., Escartin, J., & Kaus, B. (2019). Seafloor expression of oceanic detachment faulting reflects gradients in mid-ocean ridge magma supply. *Earth and Planetary Science Letters*, *516*, 176–189. https://doi.org/10.1016/j.epsl.2019.04.001

Ildefonse, B., Blackman, D. K., John, B. E., Ohara, Y., Miller, D. J., & MacLeod, C. J. (2007). Oceanic core complexes and crustal accretion at slow-spreading ridges. *Geology*, *35*(7), 623–626. https://doi.org/10.1130/G23531A.1

Jian, H., Chen, Y. J., Singh, S. C., Li, J., Zhao, M., Ruan, A., & Qiu, X. (2017). Seismic structure and magmatic construction of crust at the ultraslow-spreading Southwest Indian Ridge at 50°28′E. *Journal of Geophysical Research: Solid Earth*, *122*(1), 18–42. https://doi.org/10.1002/2016JB013377

Jian, H., Singh, S. C., Chen, Y. J., & Li, J. (2017). Evidence of an axial magma chamber beneath the ultraslow-spreading Southwest Indian Ridge. *Geology*, *45*(2), 143–146. https://doi.org/10.1130/G38356.1

Jokat, W., Kollofrath, J., Geissler, W. H., & Jensen, L. (2012). Crustal thickness and earthquake distribution south of the Logachev Seamount, Knipovich Ridge. *Geophysical Research Letters*, *39*(8), L08302. https://doi.org/10.1029/2012GL051199

Jokat, W., Ritzmann, O., Schmidt-Aursch, M. C., Drachev, S., Gauger, S., & Snow, J. (2003). Geophysical evidence for reduced melt production on the Arctic ultraslow Gakkel mid-ocean ridge. *Nature*, *423*(6943), 962–965. https://doi.org/10.1038/nature01706

Kelemen, P. B., Koga, K., & Shimizu, N. (1997). Geochemistry of gabbro sills in the crust-mantle transition zone of the Oman ophiolite: Implications for the origin of the oceanic lower crust. *Earth and Planetary Science Letters*, *146*(3–4), 475–488. https://doi.org/10.1016/S0012-821X(96)00235-X

Kempner, W. C., & Gettrust, J. F. (1982). Ophiolites, synthetic seismograms and oceanic crustal structure. *Journal of Geophysical Research*, *87*, 8447–8476. https://doi.org/10.1029/JB087iB10p08463

Klingelhöfer, F., Géli, L., Matias, L., Steinsland, N., & Mohr, J. (2000). Crustal structure of a super-slow spreading centre: A seismic refraction study of Mohns Ridge, 72°N. *Geophysical Journal International*, *141*(2), 509–526. https://doi.org/10.1046/j.1365-246X.2000.00098.x

Korenaga, J., Holbrook, W. S., Kent, G. M., Kelemen, P. B., Detrick, R. S., Larsen, H. C., et al. (2000). Crustal structure of the southeast Greenland margin from joint refraction and reflection seismic tomography. *Journal of Geophysical Research*, *105*(B9), 21591–21614. https://doi.org/10.1029/2000JB900188

Lavier, L. L., Buck, W. R., & Poliakov, A. N. (1999). Self-consistent rolling-hinge model for the evolution of large-offset low-angle normal faults. *Geology*, *27*(12), 1127–1130. https://doi.org/10.1130/0091-7613(1999)027<1127:SCRHMF>2.3.CO;2

Leroy, S., & Cannat, M. (2014a). MD 199/SISMO-SMOOTH cruise [Dataset]. *RV Marion Dufresne*. https://doi.org/10.17600/14003300

Leroy, S., & Cannat, M. (2014b). Seismic reflection profiles data from the SISMOSMOOTH 2D experiment, Southwestern Indian ridge [Dataset]. *SEANOE*. https://doi.org/10.17882/69683

Leroy, S., & Cannat, M. (2024). SISMOSMOOTH cruise—3D ocean bottom seismometer (OBS) datasets in the Southwestern Indian ridge [Dataset]. *SEANOE*. https://doi.org/10.17882/99673

Li, J., Jian, H., Chen, Y. J., Singh, S. C., Ruan, A., Qiu, X., et al. (2015). Seismic observation of an extremely magmatic accretion at the ultraslow spreading Southwest Indian Ridge. *Geophysical Research Letters*, *42*(8), 2656–2663. https://doi.org/10.1002/2014GL062521

Lin, J., Purdy, G. M., Schouten, H., Sempere, J. C., & Zervas, C. (1990). Evidence from gravity data for focused magmatic accretion along the Mid-Atlantic Ridge. *Nature*, *344*(6267), 627–632. https://doi.org/10.1038/344627a0

Lymer, G., Cresswell, D. J. F., Reston, T. J., Bull, J. M., Sawyer, D. S., Morgan, J. K., et al. (2019). 3D development of detachment faulting during continental breakup. *Earth and Planetary Science Letters*, *515*, 90–99. https://doi.org/10.1016/j.epsl.2019.03.018

MacLeod, C. J., Searle, R. C., Murton, B. J., Casey, J. F., Mallows, C., Unsworth, S. C., et al. (2009). Life cycle of oceanic core complexes. *Earth and Planetary Science Letters*, *287*(3–4), 333–344. https://doi.org/10.1016/j.epsl.2009.08.016

Magde, L. S., & Sparks, D. W. (1997). Three-dimensional mantle upwelling, melt generation, and melt migration beneath segments of slow spreading ridges. *Journal of Geophysical Research*, *102*(B9), 20571–20583. https://doi.org/10.1029/97JB01278

Malvoisin, B., Carlut, J., & Brunet, F. (2012). Serpentinization of oceanic peridotites: 1. A high-sensitivity method to monitor magnetite production in hydrothermal experiments. *Journal of Geophysical Research*, *117*(B1), B01104. https://doi.org/10.1029/2011JB008612

Martin, B., & Fyfe, W. S. (1970). Some experimental and theoretical observations on the kinetics of hydration reactions with particular reference to serpentinization. *Chemical Geology*, *6*, 185–202. https://doi.org/10.1016/0009-2541(70)90018-5

Miller, D. J., & Christensen, N. I. (1997). Seismic velocities of lower crustal and upper mantle rocks from the slow-spreading Mid-Atlantic Ridge, south of the Kane Transform Zone (MARK). In *Proceedings-Ocean Drilling Program Scientific Results* (pp. 437–456). National Science Foundation.

Minshull, T. A., Muller, M. R., Robinson, C. J., White, R. S., & Bickle, M. J. (1998). Is the oceanic Moho a serpentinization front? *Geological Society - Special Publications*, *148*(1992), 71–80. https://doi.org/10.1144/GSL.SP.1998.148.01.05

Minshull, T. A., Muller, M. R., & White, R. S. (2006). Crustal structure of the Southwest Indian Ridge at 66°E: Seismic constraints. *Geophysical Journal International*, *166*(1), 135–147. https://doi.org/10.1111/j.1365-246X.2006.03001.x

Minshull, T. A., & White, R. S. (1996). Thin crust on the flanks of the slow-spreading Southwest Indian Ridge. *Geophysical Journal International*, *125*(1), 139–148. https://doi.org/10.1111/j.1365-246X.1996.tb06541.x

Momoh, E., Cannat, M., & Leroy, S. (2020). Internal structure of the oceanic lithosphere at a melt-starved ultraslow-spreading mid-ocean ridge: Insights from 2-D seismic data. *Geochemistry, Geophysics, Geosystems*, *21*(2), e2019GC008540. https://doi.org/10.1029/2019GC008540

Momoh, E., Cannat, M., Watremez, L., Leroy, S., & Singh, S. C. (2017). Quasi-3-D seismic reflection imaging and wide-angle velocity structure of nearly amagmatic oceanic lithosphere at the ultraslow-spreading Southwest Indian ridge. *Journal of Geophysical Research: Solid Earth*, *122*(12), 9511–9533. https://doi.org/10.1002/2017JB014754

Muller, M. R., Minshull, T. A., & White, R. S. (1999). Segmentation and melt supply at the Southwest Indian Ridge. *Geology*, *27*(10), 867–870. https://doi.org/10.1016/S0012-821X(97)00030-7

Muller, M. R., Minshull, T. A., & White, R. S. (2000). Crustal structure of the Southwest Indian Ridge at the Atlantis II fracture zone. *Journal of Geophysical Research*, *105*(B11), 25809–25828. https://doi.org/10.1029/2000JB900262

Muller, M. R., Robinson, C. J., Minshull, T. A., White, R. S., & Bickle, M. J. (1997). Thin crust beneath ocean drilling program borehole 735B at the Southwest Indian Ridge? *Earth and Planetary Science Letters*, *148*(1–2), 93–107. https://doi.org/10.1016/s0012-821x(97)00030-7

Mutter, C. Z., & Mutter, J. C. (1993). Variations in thickness of layer 3 dominate oceanic crustal structure. *Earth and Planetary Science Letters*, *117*(1–2), 295–317. https://doi.org/10.1016/0012-821X(93)90134-U

Natland, J. H., & Dick, H. J. (2009). Paired melt lenses at the East Pacific Rise and the pattern of melt flow through the gabbroic layer at a fast-spreading ridge. *Lithos*, *112*(1–2), 73–86. https://doi.org/10.1016/j.lithos.2009.06.017

Parmentier, E., & Morgan, J. (1990). Spreading rate dependence of three-dimensional structure in oceanic spreading centres. *Nature*, *348*(6299), 325–328. https://doi.org/10.1038/348325a0

Parnell-Turner, R. E., Mittelstaedt, E., Kurz, M. D., Jones, M. R., Soule, S. A., Klein, F., et al. (2018). The final stages of slip and volcanism on an oceanic detachment fault at 13° 48′N, mid-Atlantic Ridge. *Geochemistry, Geophysics, Geosystems*, *19*(9), 3115–3127. https://doi.org/10.1029/2018GC007536

Parnell-Turner, R. E., Sohn, R., Peirce, C., Reston, T., MacLeod, C., Searle, R., & Simão, N. (2017). Oceanic detachment faults generate compression in extension. *Geology*, *45*(10), 923–926. https://doi.org/10.1130/g39232.1

Peirce, C., Grevemeyer, I., Hayman, N. W., & Van Avendonk, H. J. A. (2022). Active ocean–continent transform margins: Seismic investigation of the Cayman Trough-Swan Island ridge-transform intersection. *Geophysical Journal International*, *229*(3), 1604–1627. https://doi.org/10.1093/gji/ggac019

Peirce, C., Robinson, A. H., Campbell, A. M., Funnell, M. J., Grevemeyer, I., Hayman, N. W., et al. (2019). Seismic investigation of an active ocean–continent transform margin: The interaction between the Swan Islands Fault Zone and the ultraslow-spreading Mid-Cayman Spreading Centre. *Geophysical Journal International*, *219*(1), 159–184. https://doi.org/10.1093/gji/ggz283

Phipps Morgan, J., & Chen, Y. J. (1993). The genesis of oceanic crust: Magma injection, hydrothermal circulation, and crustal flow. *Journal of Geophysical Research*, *98*(B4), 6283–6297. https://doi.org/10.1029/92JB02650

Purdy, G. M., Kong, L. S. L., Christeson, G. L., & Solomon, S. C. (1992). Relationship between spreading rate and the seismic structure of mid-ocean ridges. *Nature*, *355*(6363), 815–817. https://doi.org/10.1038/355815a0

Reston, T. J. (2018). Flipping detachments: The kinematics of ultraslow spreading ridges. *Earth and Planetary Science Letters*, *503*, 144–157. https://doi.org/10.1016/j.epsl.2018.09.032

Reston, T. J., & McDermott, K. G. (2011). Successive detachment faults and mantle unroofing at magma-poor rifted margins. *Geology*, *39*(11), 1071–1074. https://doi.org/10.1130/G32428.1

Robinson, A. H., Watremez, L., Leroy, S., Minshull, T. A., Cannat, M., & Corbalán, A. (2024). SISMOSMOOTH cruise—3D ocean bottom seismometer (OBS) velocity models at the Southwestern Indian ridge, 64°30′E [Dataset]. *SEANOE*. https://doi.org/10.17882/100960

Rouméjon, S., & Cannat, M. (2014). Serpentinization of mantle-derived peridotites at mid-ocean ridges: Mesh texture development in the context of tectonic exhumation. *Geochemistry, Geophysics, Geosystems*, *15*(6), 2354–2379. https://doi.org/10.1002/2013GC005148

Rouméjon, S., Cannat, M., Agrinier, P., Godard, M., & Andreani, M. (2015). Serpentinization and fluid pathways in tectonically exhumed peridotites from the Southwest Indian Ridge (62–65°E). *Journal of Petrology*, *56*(4), 703–734. https://doi.org/10.1093/petrology/egv014

Sauter, D., Cannat, M., & Mendel, V. (2008). Magnetization of 0–26.5 Ma seafloor at the ultraslow spreading Southwest Indian ridge, 61°–67°E. *Geochemistry, Geophysics, Geosystems*, *9*(4), Q04023. https://doi.org/10.1029/2007GC001764

Sauter, D., Cannat, M., Rouméjon, S., Andreani, M., Birot, D., Bronner, A., et al. (2013). Continuous exhumation of mantle-derived rocks at the Southwest Indian Ridge for 11 million years. *Nature Geoscience*, *6*(4), 314–320. https://doi.org/10.1038/ngeo1771

Schlindwein, V., & Schmid, F. (2016). Mid-ocean-ridge seismicity reveals extreme types of ocean lithosphere. *Nature*, *535*(7611), 276–279. https://doi.org/10.1038/nature18277

Simão, N. M., Peirce, C., Funnell, M. J., Robinson, A. H., Searle, R. C., Macleod, C. J., & Reston, T. J. (2020). 3-D P-wave velocity structure of oceanic core complexes at 13°N on the Mid-Atlantic Ridge. *Geophysical Journal International*, *221*(3), 1555–1579. https://doi.org/10.1093/gji/ggaa093

Sinton, J. M., & Detrick, R. S. (1992). Mid-Ocean ridge magma chambers. *Journal of Geophysical Research*, *97*(B1), 197–216. https://doi.org/10.1029/91JB02508

Smith, D. K., & Cann, J. R. (1999). Constructing the upper crust of the Mid-Atlantic Ridge: A reinterpretation based on the Puna Ridge, Kilauea Volcano. *Journal of Geophysical Research*, *104*(B11), 25379–25399. https://doi.org/10.1029/1999JB900177

Smith, D. K., Cann, J., & Escartín, J. (2006). Widespread active detachment faulting and core complex formation near 13°N on the Mid-Atlantic Ridge. *Nature*, *442*(7101), 440–443. https://doi.org/10.1038/nature04950

Sparks, D. W., Parmentier, E. M., & Morgan, J. P. (1993). Three-dimensional mantle convection beneath a segmented spreading center: Implications for along-axis variations in crustal thickness and gravity. *Journal of Geophysical Research*, *98*(B12), 21977–21995. https://doi.org/10.1029/93JB02397

Tolstoy, M., Harding, A. J., & Orcutt, J. A. (1993). Crustal thickness on the Mid-Atlantic Ridge: Bull's-Eye gravity anomalies and focused accretion. *Science*, *262*(5134), 726–729. https://doi.org/10.1126/science.262.5134.726

Tucholke, B. E., Lin, J., & Kleinrock, M. C. (1998). Megamullions and mullion structure defining oceanic metamorphic core complexes on the Mid-Atlantic Ridge. *Journal of Geophysical Research*, *103*(B5), 9857–9866. https://doi.org/10.1029/98JB00167

Van Avendonk, H. J., Hayman, N. W., Harding, J. L., Grevemeyer, I., Peirce, C., & Dannowski, A. (2017). Seismic structure and segmentation of the axial valley of the Mid-Cayman Spreading Center. *Geochemistry, Geophysics, Geosystems*, *18*(6), 2149–2161. https://doi.org/10.1002/2017gc006873

Wang, Z., & Singh, S. C. (2022). Seismic evidence for uniform crustal accretion along slow-spreading ridges in the equatorial Atlantic Ocean. *Nature Communications*, *13*(1), 7809. https://doi.org/10.1038/s41467-022-35459-z

Wessel, P., Luis, J. F., Uieda, L., Scharroo, R., Wobbe, F., Smith, W. H. F., & Tian, D. (2019). The Generic Mapping Tools version 6. *Geochemistry, Geophysics, Geosystems*, *20*(11), 5556–5564. https://doi.org/10.1029/2019GC008515

White, R. S., Minshull, T. A., Bickle, M. J., & Robinson, C. J. (2001). Melt generation at very slow-spreading oceanic ridges: Constraints from geochemical and geophysical data. *Journal of Petrology*, *42*(6), 1171–1196. https://doi.org/10.1093/petrology/42.6.1171

Zelt, C. A. (1998). Lateral velocity resolution from three-dimensional seismic refraction data. *Geophysical Journal International*, *135*(3), 1101–1112. https://doi.org/10.1046/j.1365-246X.1998.00695.x

Zelt, C. A., & Barton, P. J. (1998). Three-dimensional seismic refraction tomography: A comparison of two methods applied to data from the Faeroe Basin. *Journal of Geophysical Research: Solid Earth*, *103*(4), 7187–7210. https://doi.org/10.1029/97jb03536

Zhou, F., Dyment, J., Tao, C., & Wu, T. (2022). Magmatism at oceanic core complexes on the ultraslow Southwest Indian Ridge: Insights from near-seafloor magnetics. *Geology*, *50*(6), 726–730. https://doi.org/10.1130/G49771.1